

# Representing the Global-Scale Water Masses in Ocean General Circulation Models

MATTHEW H. ENGLAND

*Department of Geology and Geophysics, The University of Sydney, Sydney, Australia*

(Manuscript received 11 February 1992, in final form 4 November 1992)

## ABSTRACT

A hierarchy of coarse-resolution World Ocean experiments were integrated with a view to determining the most appropriate representation of the global-scale water masses in ocean general circulation models. The largest-scale response of the simulated ocean to the prescribed forcing in each model run is described. The World Ocean model eventually has a realistic approximation of continental outlines and bottom bathymetry. The model forcing at the sea surface is derived from climatological fields of temperature, salinity, and wind stress. The first experiment begins with a quite unrealistic and idealized World Ocean. Subsequent experiments then employ more realistic surface boundary conditions, model geometry, and internal physical processes. In all, 16 changes to the model configuration are investigated.

A fundamental dynamical constraint in the Drake Passage gap appears to limit the outflow rate of bottom water in the Antarctic region. This constraint acts to *decouple* the extreme Antarctic waters from the rest of the World Ocean. In a similar manner, including a surface wind stress acts to decouple the two hemispheres by limiting near-surface meridional flows across the equator. In the Atlantic basin, this decoupling becomes negligible when North Atlantic Deep Water (NADW) production is simulated. It is found that the representation of low salinity Antarctic Intermediate Water (AAIW) is sensitive to the level of horizontal diffusion employed by the model, as well as the chosen geometry of the Drake Passage gap and the amount of buoyancy provided by the model's deep water. For example, provided that lateral diffusion rates are not too excessive, a fresh tongue of AAIW is simulated if either sufficiently dense bottom water is formed off Antarctica, or if enough NADW outflows into the Southern Ocean. The inclusion of an isopycnal mixing scheme is shown to improve the representation of AAIW in coarse-resolution models.

The rate of horizontal diffusion and the relative location of the Drake Passage gap to the polar westerlies determines the shape and strength of an intense meridional overturning cell in the Southern Ocean. The inclusion of an isopycnal mixing scheme does not affect this circulation pattern significantly. On the other hand, the intensification of NADW production can substantially weaken the downwelling component of this cell by drawing more water of Southern Ocean origin northward. Accurately simulating NADW production and outflow requires a complete seasonal cycle in thermohaline forcing in the North Atlantic. The return path of NADW is primarily via a "cold water route" (i.e., the Drake Passage), although sufficiently strong NADW formation sees some return flow via the Agulhas leakage (i.e., the "warm water route"). By the last experiment of the present study, the model reproduces the subtle vertical layering of deep and intermediate water masses quite accurately. This represents a major success for the coarse-resolution multilevel ocean model.

## 1. Introduction

The distribution of heat and salt in the World Ocean has been investigated extensively in recent decades, both in observational analyses and theoretical modeling. As part of a broad scientific program to understand the world's climate, much effort in the oceanographic community is presently being directed at quantifying the global-scale transports of heat and fresh water in the ocean. Ultimately, the formation of the world's water masses is inherently linked to global climate through these large-scale oceanic transports of heat and fresh water. The central goal of this study is to employ a global-scale model of the ocean general

circulation to investigate the processes that determine the water mass distribution of the World Ocean.

Prior to the development of an ocean general circulation model (GCM) of the World Ocean (Bryan and Lewis 1979), the thermohaline component of the ocean circulation had been largely neglected in theoretical studies. This was largely due to the difficulty of incorporating nonlinear processes (such as convective overturn) in analytic models. More recently, however, the worldwide availability of the Geophysical Fluid Dynamics Laboratory (GFDL) ocean GCM (Cox 1984; Pacanowski et al. 1991) has seen a rapid increase in the number of studies that deal directly with the component of thermohaline circulation in the ocean. Many of these studies are carried out over idealized single basin geometries (e.g., Bryan 1986; Weaver and Sarachik 1990, 1991; Cummins 1991; Weaver et al. 1991), revealing interesting features in the stability and

---

Corresponding author address: Dr. Matthew H. England, GRGS/CNRS, 18 Avenue Edouard Belin, 31055, Toulouse, Cedex, France.

maintenance of the ocean's thermohaline circulation. However, to study the world's climate on time scales longer than a year, it is necessary to consider the entire atmosphere coupled to the ocean on a global scale. As such, it is useful to investigate general circulation models of the World Ocean that are forced by known climatological surface conditions.

A rather novel approach at understanding the mechanisms responsible for the largest-scale features of the global water mass structure was pursued by Cox (1989). He presented a series of four *idealized* World Ocean experiments that varied sequentially in some fundamental way. In short, he began with a model ocean that had a closed Drake Passage, only thermohaline forcing of the sea surface, and a fresh North Atlantic. In the subsequent experiments, he opened the Drake Passage (experiment II), applied surface wind forcing (experiment III) and gave the North Atlantic enhanced near-surface salinities (experiment IV). With such an approach, he was able to isolate (amongst other things) the response of the global-scale water masses to the establishment of the Antarctic Circumpolar Current (ACC) in experiments II and III.

The present study is in a similar form to the simulations conducted by Cox (1989), in that we investigate a series of numerical experiments that sequentially employ more realistic boundary conditions and internal physical processes. One fundamental difference between the study of Cox (1989) and the present series of experiments is that we employ realistic bottom bathymetry and continental outlines. Furthermore, we examine a greater range of modifications to the model configuration. In the first experiment, we begin with a quite unrealistic World Ocean; the Drake and Indonesian passages are closed, there is only an annually averaged and zonally averaged thermohaline forcing of the sea surface, and temperature and salinity are mixed horizontally without consideration of the ocean's tendency to mix tracers along surfaces of constant density. By the last experiment reported in the present study, we have resolved throughflows in the Drake and Indonesian passages, there is realistic thermohaline and wind-stress forcing of the sea surface, and tracers are being mixed predominantly along surfaces of constant density. In all, we investigate the response of the simulated water mass structure to *sixteen* changes in the model configuration and surface forcing. An initial report of some of the findings in the present series of experiments is found in England (1992a).

Primitive equation models display a range of deficiencies at coarse resolution. For example, the thermocline tends to be too deep and diffuse (Bryan 1979). Decreasing the vertical diffusivity with a view to tightening the simulated pycnocline in turn weakens the modeled thermohaline circulation and poleward heat transport (Bryan 1987). However, coarse-resolution ocean GCMs will be relied upon for some time for modeling the global climate response to anthropogenic

changes in the world's environment, even with today's rapid advances in parallel-processing technology. The present study is one of a whole range (e.g., Toggweiler et al. 1989; Meehl et al. 1982; Bryan and Lewis 1979) that hope to evaluate existing coarse-resolution ocean models that have been coupled to the atmosphere in order to study global climate.

The study of the ocean's water masses is intimately related to climate through the global heat and freshwater budgets. At coarse resolution, we cannot hope to capture some of the fine water mass structure observed in the real ocean. However, it is hoped that the *global-scale* water masses can be resolved in the present study without requiring enhanced horizontal or vertical resolution. By global-scale water masses, we refer to those water masses that exist on a basin to interbasin scale; namely, North Atlantic Deep Water (NADW), Antarctic Bottom Water (AABW), and Antarctic and North Pacific Intermediate Water (AAIW, NPIW). In a *coupled* configuration, coarse-resolution ocean models have failed to represent some of these water masses (England et al. 1992). In a *decoupled* mode with only annual-mean surface conditions, the representation is by no means improved (e.g., Toggweiler et al. 1989). On the other hand, by tuning the model boundary conditions and internal physical processes, we hope to represent the global-scale water masses without resorting to higher resolution or semidiagnostic internal forcing.

## 2. Model description

The ocean model employed in this study is the multilevel numerical model described by Bryan (1969) and adapted to modern vectorizing computers by Cox (1984) and Pacanowski et al. (1991) at the GFDL. The model domain consists of a global coverage of the World Ocean. The grid spacing is  $3.75^\circ$  longitude by  $4.5^\circ$  latitude with 12 unequally spaced vertical levels (at depths listed in Table 3) matching the resolution used in the standard GFDL climate model (e.g., Manabe et al. 1991). Apart from variations in the bathymetry through the Drake and Indonesian Passages, the bottom topography is invariant between experiments. The bathymetry represents a smoothed discretized version of the real World Ocean bottom topography. The smoothing is necessary to ensure convergence of the model's barotropic streamfunction (Killworth 1987; Cox 1984). In most of the experiments, the model domain only covers the open oceans, and no consideration is made of the outflow from inland seas such as the Mediterranean Sea or the Great Lakes of North America. However, in some of the later experiments, the Mediterranean Sea is included in the model domain, and the adjoining North Atlantic and Mediterranean water columns are made to mix horizontally and completely to a depth of 1347 m across the (unresolved) Strait of Gibraltar (after Manabe et

al. 1991). Maps of the bathymetry and continental boundaries covering each of the 12 experiments are presented in Fig. 1.

Because of the coarse horizontal and vertical resolution, the effects of mesoscale eddies are only taken into account implicitly by approximate closure schemes. In all experiments, the horizontal ( $A_{MH}$ ) and vertical ( $A_{MV}$ ) viscosity coefficients are taken to be constants independent of depth. These and other parameters are quantified in Table 2. To minimize numerical instabilities in cross-equatorial meridional flows (Weaver and Sarachik 1990), we employ a rather large vertical viscosity.

Contrasting the use of spatially uniform viscosity coefficients, we have chosen to employ depth-dependent horizontal, vertical, and isopycnal diffusivities. In all experiments, we employ a vertical mixing coefficient ( $A_{HV}$ ) that is lowest within the surface layer and increases below the thermocline (following Bryan and Lewis 1979) according to the relation

$$A_{HV}(z) = A_* + A_r \tan^{-1}[\lambda(z - z_*)], \quad (1)$$

where  $A_*$  is the vertical diffusion coefficient at a reference depth  $z = z_*$  and  $A_r$  defines the range of  $A_{HV}$  from the surface to the bottom. The value of  $\lambda$  defines the rate at which  $A_{HV}$  varies with depth, particularly near the depth  $z_*$ . While the values of  $A_{HV}$  remain fixed for the core experiments reported in the present study (increasing from  $0.3 \text{ cm}^2 \text{ sec}^{-1}$  in the upper kilometer to  $1.3 \text{ cm}^2 \text{ s}^{-1}$  in the deepest layer), we also report the effects of larger deep vertical diffusivities advocated by Cummins (1991).

The depth dependence of horizontal diffusivity ( $A_{HH}$ ) is taken to reflect the ocean's tendency to diffuse more rapidly at the surface than at depth, which can be parameterized (following Bryan and Lewis 1979) as

$$A_{HH}(z) = A_{BH} + (A_{SH} - A_{BH}) \exp(-z/500). \quad (2)$$

Similarly, when incorporating an isopycnal diffusion of temperature and salinity it is more realistic to adopt a simple depth dependence for the rate of effective isopycnal mixing. So, we take the isopycnal mixing coefficient ( $A_{HI}$ ) to be

$$A_{HI}(z) = A_{BI} + (A_{SI} - A_{BI}) \exp(-z/500). \quad (3)$$

In the notation used in Eqs. (2) and (3), the horizontal diffusion decreases from its maximum value of  $A_{SH}$  at the surface to  $A_{BH}$  at the bottom layer, while the isopycnal diffusion decreases from  $A_{SI}$  at the surface level to  $A_{BI}$  at the bottom.

In earlier experiments, the mixing of tracers takes place purely in Cartesian coordinates, with relatively high rates of lateral diffusion and without regard to the orientation of isopycnal surfaces. In some regions of the World Ocean such as the Southern Ocean, this implies an unrealistically strong diapycnal (i.e., cross iso-

pycnal) mixing of temperature and salinity. Nevertheless, the inclusion of an isopycnal mixing scheme like that of Redi (1982) increases the computational requirements of the model quite significantly (each time step requires approximately 50% more CPU time with an isopycnal configuration). Furthermore, the high rate of lateral diffusion ensures a more rapid convergence of the model to steady state. In short, the early experiments involve unrealistic diffusion in the horizontal in order to ensure relatively low computational requirements. After some preliminary experiments, the lateral diffusivity is scaled down significantly (Table 2). This is shown to improve the representation of water masses in the model. In the later experiments, we employ an even weaker background Cartesian mixing (for numerical stability), and incorporate an isopycnal mixing scheme (Redi 1982; Cox 1987) that more realistically represents the tendency for heat and salt to be mixed on surfaces of constant density. Following Manabe et al. (1991), the rate of isopycnal diffusion decreases from  $5.0 \times 10^7 \text{ cm}^2 \text{ s}^{-1}$  in the surface layer down to  $1.0 \times 10^7 \text{ cm}^2 \text{ s}^{-1}$  at the bottom [according to Eq. (3)]. This roughly corresponds to estimates of effective isopycnal mixing in the real ocean (e.g., Thiele et al. 1986; McWilliams et al. 1983).

The prognostic variables of the model are potential temperature (hereinafter referred to as temperature,  $T$ ), salinity ( $S$ ), and the two horizontal velocity components ( $u$ ,  $v$ ). The vertical velocity component ( $w$ ) is a diagnostic variable determined by the continuity equation. No passive tracers are carried by the model, partly to save on computational load. The rigid-lid approximation is made at the sea surface, and no-slip and insulating boundary conditions are applied at horizontal boundaries. The bottom is also assumed to be insulating, although a linear drag relationship simulates the effects of bottom friction by generating weak stresses in response to horizontal motion in the bottom layer. The method of convective adjustment of unstable parts of the water column follows the technique described by Bryan and Lewis (1979). Whenever the water column becomes unstable, temperature and salinity are mixed vertically over the unstable portion of the water column. Heat and salt are conserved in this process by mixing adjacent unstable levels completely. While some recent studies have shown the parameterization of convection to be important in determining the simulated ocean thermohaline circulation (e.g., Marotzke 1991), we found negligible adjustment of our model solutions on a switch in convection schemes.

The ocean is forced at the sea surface by climatological boundary conditions of temperature, salinity, and wind stress. The atmosphere to ocean momentum flux is determined from the annual mean wind stress climatology of Hellerman and Rosenstein (1983) interpolated onto the model grid points. The effective surface fluxes of heat and fresh water are implied by restoring the model's surface layer temperature and

# TOPOGRAPHY

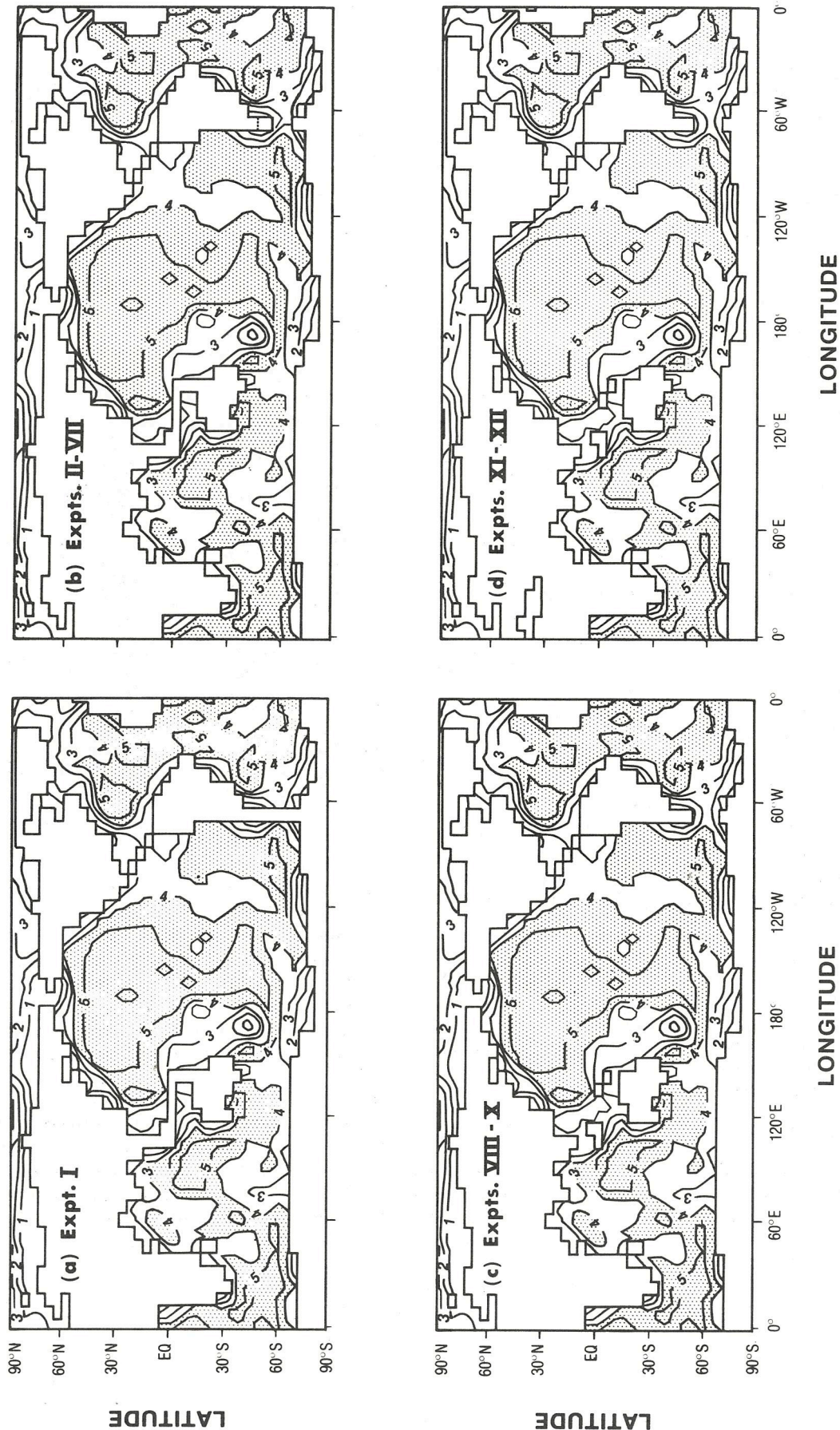


FIG. 1. Continental outlines and ocean bathymetry in the 12 core experiments. Depth contours are shown in kilometers. The dashed line at Cape Horn indicates the southward extent of South America in the wide Drake Passage experiments (experiments II-IV).

salinity toward the long-term mean climatology of Levitus (1982). In certain experiments, seasonal fluctuations in surface heat and freshwater fluxes are crudely represented by referencing the Levitus (1984, 1986) seasonal climatology. In general, the surface relaxation time scale is  $(30 \text{ days})^{-1}$  for temperature and  $(50 \text{ days})^{-1}$  for salinity. The technique of restoring modeled surface temperatures toward observed values (via a Newtonian damping law) was first justified by Haney (1971) on the grounds that there is a direct feedback between oceanic surface temperatures and atmospheric (forcing) temperatures above the sea surface. However, there is no physical justification for using an equivalent technique to force the model's surface salinities because the freshwater flux (i.e., precipitation plus runoff minus evaporation) is essentially independent of the surface salinity. A more appropriate boundary condition on salinity would be derived from a fixed freshwater flux (Welander 1986; Weaver and Sarachik 1991). However, most *global-scale* ocean modeling studies continue to employ restoring boundary conditions on both temperature and salinity (e.g., Toggweiler et al. 1989; Semtner and Chervin 1992; Hirst and Godfrey 1993), including all but one experiment in the present study. One reason for this is that available climatological datasets for global evaporation and precipitation are derived from relatively sparse and infrequent sampling (e.g., Baumgartner and Reichel 1975) and are therefore fairly unreliable. In fact, recent estimates of evaporation minus precipitation over the North Atlantic (e.g., Isemer and Hasse 1987; Schmitt et al. 1989) differ in area integral by up to  $4 \times 10^5 \text{ m}^3 \text{ s}^{-1}$  (Schmitt and Bryan 1991), a discrepancy that exceeds the estimated freshwater loss from the North Atlantic (e.g.,  $2.6 \times 10^5 \text{ m}^3 \text{ s}^{-1}$ , Wijffels et al. 1992). An uncertainty of  $4 \times 10^5 \text{ m}^3 \text{ s}^{-1}$  in net freshwater loss represents more than twice the outflow rate of the Amazon river (Schmitt and Bryan 1991). Furthermore, the North Atlantic is the most densely observed ocean basin in the World, so we can expect even greater uncertainty elsewhere. Another consideration is that ocean GCMs forced with *mixed* boundary conditions (i.e., restoring on temperature, fixed-flux on salinity) tend to behave rather erratically (e.g., Bryan 1986; Weaver and Sarachik 1991).

In none of the experiments presented here do we restore internal temperatures or salinities. This has been a popular technique to reduce the required computational effort to achieve steady state in the initial stages of some fine-resolution models (e.g., Semtner and Chervin 1988; Saunders and Thompson 1993), because convergence does not depend on slow mixing processes and ventilation of the deep ocean. The internal restoring terms also ensure that the model representation of temperature and salinity remains close to observed values. However, in a robust diagnostic or even semidiagnostic mode, the intermediate and deep water masses need not be formed at the surface by

convective overturn and mixing processes; they can originate unrealistically from those interior grid points being relaxed to observations. Toggweiler et al. (1989) found that a purely prognostic version of the GFDL ocean GCM produced a superior deep ocean circulation to a robust diagnostic realization because the weak interior restoring terms tend to suppress convection and other vertical motions. Furthermore, as Cox (1989) notes, the imposition of known water masses upon a model *a priori* fundamentally limits the model's capacity to be used to study their formation.

### 3. Experimental procedure

A sequence of experiments was initially designed to study the response of the model ocean to changes in surface boundary conditions, model geometry, and mixing parameterization. Ultimately, however, this sequence was augmented and redesigned in view of the simulation obtained at the end of each experiment. In this sense, the experimental procedure devolved into an attempt to improve the model's water mass representation by adjusting the model configuration in some appropriate way. In several instances, the water mass representation was little affected by such an adjustment; in others a marked improvement was realized. It is clearly impossible in such a study to know *a priori* the optimum experimental procedure. It was decided that this article report not only the experiments that saw a significant improvement in water mass representation; but also several that had a negligible or even negative effect on the quality of the modeled  $T$ - $S$ .

Table 1 shows a chronology of the numerical experiments reported in the present study. Only experiments I and II are spun up from an initially isothermal ( $5.0^\circ\text{C}$ ) ocean at rest with uniform salinity (34.70 psu). The other cases follow on from steady or quasi steady states obtained in previous experiments. The acceleration technique of Bryan (1984) is used to speed up the convergence of the deeper layers of the model by employing asynchronous time stepping. The barotropic streamfunction and baroclinic velocity equations are integrated with a time step of 20 minutes. The time step for the  $T$  and  $S$  equations varies from just over 1 day in the upper 1 km of the model ocean to about 5 days at level 12. The surface integration times required for each run are included in Table 1. Each experiment was eventually run out so that there was negligible long-term drift in the temperature, salinity, and circulation fields. Because it is both costly and unnecessary to integrate to a completely equilibrated solution, we chose to define a convergence criterion that reflected a sufficiently steady-state solution. We considered each experiment to be sufficiently converged provided that the global mean temperature and salinity changes were less than  $0.01^\circ\text{C}$  and  $0.004 \text{ psu}$  per century at each of the 12 vertical levels. Extensive checks on the conservation of heat and salt at individual ocean grid points indicate

TABLE 1. Chronology of the numerical experiments reported in the present study, including the effective integration time of the surface levels. The deeper layers of the model are effectively integrated five times as long through the acceleration technique of split time-stepping (Bryan 1984). Also included is an identifying feature of each experiment and a brief synopsis of the lateral diffusion rate and surface forcing conditions. (BC: Boundary conditions, NA: North Atlantic, NP: North Pacific,  $S_{adj}$ : salinity adjustment of Antarctica).

Experiment	Identifying feature	Surface integration time (years)	Horizontal diffusion	Surface forcing
I	Drake Passage closed	1340	High $A_{HH}$	Zonal, thermohaline
II	Open the Drake Passage	1450	High $A_{HH}$	Zonal, thermohaline
III	Apply surface wind stress	740	High $A_{HH}$	Zonal
IV	Enhanced Antarctic salinity	920	High $A_{HH}$	Zonal, Antarctic $S_{adj}$
V	Narrow Drake Passage	430	High $A_{HH}$	Zonal, Antarctic $S_{adj}$
VI	Decrease horizontal diffusion	870	Low $A_{HH}$	Zonal, Antarctic $S_{adj}$
VII	Enhanced NA salinity	840	Low $A_{HH}$	NA/NP $S$ , winter $S_{adj}$
VIII	Open Indonesian Passage	460	Low $A_{HH}$	NA/NP $S$ , winter $S_{adj}$
IX	Isopycnal mixing	610	$A_{HI}$ , weak $A_{HH}$	NA/NP $S$ , winter $S_{adj}$
X	Zonally varying BCs	520	$A_{HI}$ , weak $A_{HH}$	Levitus $T/S$ , weak $S_{adj}$
XI	Cut off $S_{adj}$	770	$A_{HI}$ , weak $A_{HH}$	Levitus $T/S$
XI (mixed)	Mixed BCs	400	$A_{HI}$ , weak $A_{HH}$	Levitus $T$ , implied $S$ flux
XII	Seasonal NA forcing	970	$A_{HI}$ , weak $A_{HH}$	Seasonal $NA$ , weak $S_{adj}$

that the only time-dependent aspect of the converged solution is related to intermittent episodes of convective adjustment. Once the convergence criterion is reached, the acceleration method of split time stepping (Bryan 1984) is switched off, and the experiment is run out a further ten years (with reduced time steps) to check the stability of the asynchronous state. In no instances did the solution become unstable during this switch from asynchronous to synchronous time stepping.

A more detailed description of the present series of experiments can be found in England (1992b). For this study, we limit the description of the experimental procedure to an account of the changes effected in each model run. In the first experiment, the World Ocean model includes no wind forcing at the sea surface and no direct connection between the Pacific and Atlantic basins (i.e., the Drake Passage is closed). The Indonesian Passage is also blocked off completely (Fig. 1a). The thermohaline forcing at the sea surface is implied by restoring surface-layer temperatures and salinities towards the annually averaged and zonally averaged Levitus (1982) climatology. Experiment II is identical to the first experiment in every way except that the Drake Passage is open, enabling the existence of a circumpolar current. In experiment III, a wind stress is applied at the ocean surface. The wind stress applied represents an idealized form of the annually averaged and zonally averaged climatology of Hellerman and Rosenstein (1983). Including a wind stress at the sea

surface enhances the total kinetic energy density in the simulated ocean (a sixfold increase is realized), and correspondingly the ventilation of the deep ocean occurs somewhat faster than in the thermohaline experiments (experiments I and II). This shortens the integration times required to meet the convergence criteria (Table 1).

The world's deep water masses are formed at high latitudes when air-sea or sea-ice interaction leaves the surface water sufficiently dense to sink to great depths. This process generally occurs in the winter hemisphere, for it is during winter that the ocean releases heat into the atmosphere, and when sea-ice formation rejects salt into the water column. To evaluate the role of wintertime AABW formation in determining the World's water mass distribution, experiment IV is integrated with an imposed high surface salinity adjacent to Antarctica (south of 65°S). The southernmost row of ocean grid points is restored towards a maximum value of 35.00 psu with a smooth interpolation defining the enhanced forcing at the remaining latitudes up to 65°S. The maximum surface salinity chosen approximately matches estimates of the wintertime salinity of shelf water in the Ross and Weddell seas (Jacobs et al. 1985; Foster and Carmack 1976).

The role of the Drake Passage bathymetry is studied in experiment V by adjusting the model's continental boundaries so that the ocean's "barrier-free zone" is more realistically poleward of the maximum westerly

wind belt. The conventional GFDL climate model has an artificially wide Drake Passage that infringes on the latitudes of strong westerly wind stress, forcing deep meridional overturning to compensate near-surface Ekman transport (e.g., Toggweiler et al. 1989; Stouffer et al. 1989; Manabe et al. 1991). The resulting ventilation of the deep ocean in this region significantly moderates the simulated climate response to a gradual increase in atmospheric  $\text{CO}_2$  (e.g., Stouffer et al. 1989; Manabe et al. 1991). By better representing the Drake Passage bathymetry (in particular, by extending the tip of South America one grid point poleward), we extend the region where a significant zonal pressure gradient can exist. In this case, more of the near-surface Ekman transport can be balanced by geostrophic return flow in the upper ocean, and the deep ventilation will weaken.

Until experiment V, the horizontal diffusion in the experiments has been excessive, allowing relatively rapid convergence of the simulated ocean to a steady state. Experiment VI is designed to provide a measure of the model's sensitivity to variations in the rate of lateral diffusion. It is identical to experiment V in every respect except that the horizontal diffusion coefficient is decreased substantially (Table 2). Corresponding to the decrease in lateral diffusion rates, the adjustment processes in the deep ocean become somewhat slower, requiring longer integration times to bring the model to a converged state.

Experiment VII was developed with a view to including NADW formation in the model solution. To distinguish between the relative saltiness of the North Atlantic and freshness of the North Pacific, experiment VII is integrated with Northern Hemisphere surface salinities restored to the annually averaged and *basin-averaged* salinity fields of Levitus (1982). Furthermore, to weaken the dominance of AABW in the earlier experiments, experiment VII moderates the salinity enhancement adjacent to Antarctica to be time dependent. That is, the surface salinities are now only enhanced for three months of the year (corresponding to austral winter); otherwise the zonal mean climatology

of Levitus (1982) is adopted. Besides these two modifications in the surface salinity forcing, the experiment is identical to experiment VI.

Until experiment VII, the Indonesian Archipelago has been blocked off, allowing no direct communication between the tropical Pacific and Indian oceans. In reality, the Indonesian Passage represents an open connection between the two ocean basins, and many researchers believe the resulting throughflow to be a major component of the world's heat and freshwater balance (e.g., Gordon 1986). In experiment VIII, we open a three-gridpoint-wide Indonesian Passage by removing enough land points through the Indonesian archipelago from the bathymetry used in experiment VII (see Fig. 1). The maximum channel depth of the resulting Indonesian Passage is 1347 m (7 levels).

Up until experiment VIII, there has been no consideration of the orientation of isopycnal surfaces when computing the intensity of parameterized eddy diffusion. In the real ocean, scalar quantities (temperature, salinity, and passive tracers) are mixed rather efficiently along surfaces of constant potential density (Wüst 1933). While multilevel primitive equation models require some background Cartesian diffusion to ensure numerical stability, Redi (1982) proposed a technique to simulate the enhanced mixing of tracers along isopycnal surfaces. In experiment IX, we include this parameterization in the prognostic equations for temperature and salinity.

While the zonal asymmetry in North Pacific–North Atlantic surface salinities was recognized in experiment VII, there are other longitudinal variations in surface fluxes of heat, fresh water, and momentum. In experiment X, the forcing at the sea surface is upgraded to correspond with the annually averaged climatologies of Levitus (1982) and Hellerman and Rosenstein (1983). That is, the zonal averaging of surface conditions used up until experiment IX has been removed. The method of increasing the wintertime salinity forcing adjacent to Antarctica is maintained, though now the surface salinity is only enhanced as far north as  $69^\circ\text{S}$ .

There have been several World Ocean models documented whose forcing is simply derived from the unadjusted annual climatologies of Levitus (1982) and Hellerman and Rosenstein (1983) (e.g., Toggweiler et al. 1989; Semtner and Chervin 1988). To make comparison with these global ocean circulation models, it is useful to examine the response of the model to a cutoff in the salinity adjustment adjacent to Antarctica. Furthermore, removing the salinity enhancement will allow us to reassess its effects within the more sophisticated framework of a model employing isopycnal mixing and low horizontal diffusivities. This is carried out in experiment XI, which is identical to experiment X in every way except that there is no wintertime increase in surface salinity forcing off Antarctica. At the end of experiment XI, we go on to monitor the model's

TABLE 2. Mixing parameters used in the numerical experiments.

Parameter	Experiments I–V	Experiments VI–VIII	Experiments IX–XII
$A_{MV}$ ( $\text{cm}^2 \text{sec}^{-1}$ )	50	50	50
$A_{MH}$ ( $\text{cm}^2 \text{sec}^{-1}$ )	$2.5 \times 10^9$	$2.5 \times 10^9$	$2.5 \times 10^9$
$A_{HV}$ ( $\text{cm}^2 \text{sec}^{-1}$ )	0.3–1.3	0.3–1.3	0.3–1.3
$A_*$ ( $\text{cm}^2 \text{sec}^{-1}$ )	0.8	0.8	0.8
$A_r$ ( $\text{cm}^2 \text{sec}^{-1}$ )	$1.05/\pi$	$1.05/\pi$	$1.05/\pi$
$\lambda$ ( $\text{m}^{-1}$ )	$4.5 \times 10^{-3}$	$4.5 \times 10^{-3}$	$4.5 \times 10^{-3}$
$z_*$ (m)	2500	2500	2500
$A_{SH}$ ( $\text{cm}^2 \text{sec}^{-1}$ )	$5.0 \times 10^7$	$1.0 \times 10^7$	$0.75 \times 10^7$
$A_{BH}$ ( $\text{cm}^2 \text{sec}^{-1}$ )	$1.0 \times 10^7$	$0.5 \times 10^7$	$0.375 \times 10^7$
$A_{SI}$ ( $\text{cm}^2 \text{sec}^{-1}$ )	—	—	$5.0 \times 10^7$
			$1.0 \times 10^7$
$A_{BI}$ ( $\text{cm}^2 \text{sec}^{-1}$ )	—	—	

initial response to a switch from restoring to mixed boundary conditions.

In the final experiment (experiment XII), the role of the seasonal cycle of heat and freshwater fluxes in the North Atlantic is investigated. In the Atlantic basin north of about 30°N, the thermohaline forcing at the sea surface is derived by restoring surface-layer temperatures and salinities towards the seasonal distribution of Levitus (1984, 1986). By including the seasonal cycle in temperature, the model should form more NADW because the minimum wintertime temperatures will be realized. Similarly, higher wintertime surface salinities (Levitus 1986) will ensure enhanced surface layer densities in the North Atlantic during winter. In the version of experiment XII reported here, we also reintroduce a weak form of the Antarctic salinity adjustment first employed in experiment IV. In particular, during July and August only, the surface salinity of the southernmost row of ocean grid points is restored towards a maximum value of 34.90 psu, with a smooth interpolation defining the enhanced forcing at the remaining latitudes up to 69°S.

A range of other sensitivity experiments have also been investigated and from time to time they will be referred to during the evaluation of the core experiments.

#### 4. Modeled circulation and water mass formation

The globally averaged and annually averaged volume-weighted temperature-salinity profiles obtained in each of the 12 experiments are presented in Table 3. Included for comparison are the observed long-term mean global  $T$ - $S$  profiles reported by Levitus (1982). This table provides a useful reference for monitoring the largest-scale response of the world's water masses to each fundamental change prescribed during the course of the experiments. Global-scale responses are realized when a first-order change to the model configuration is made, or when a strong source of deep-water formation is introduced. For example, introducing an artificial source of salty water in the extreme Southern Ocean (experiment IV) substantially increases the salt content of the entire ocean. Introducing a global surface wind stress (experiment III) significantly deepens the thermocline, and warms the bottom layers due to the enhanced ventilation of the deep ocean. In contrast, second-order modifications to the model configuration (e.g., narrowing the Drake Passage gap by one grid point) only slightly alter the global mean profiles.

The digitized global mean  $T$ - $S$  profiles for each experiment also clarify the characteristics of bottom and intermediate water formed in the model. For example, with no salinity adjustment adjacent to Antarctica (experiments I-III, XI), the model's bottom water is too fresh. Furthermore, the salinity adjustment appears to

TABLE 3a. Globally averaged temperature profiles simulated in Experiments I-XII, as well as the corresponding profile interpolated from the annually and globally averaged Levitus (1982) climatology.

Depth (m)	$T$ (obs) (°C)	$T$ (°C)											
		I	II	III	IV	V	VI	VII	VIII	IX	X	XI	XII
1	25.45	17.81	17.81	17.81	17.81	17.81	17.81	17.80	17.82	17.82	17.75	17.75	17.62
2	85.10	15.43	15.41	15.77	15.78	15.74	16.09	16.03	16.13	15.78	16.10	16.15	15.90
3	169.50	14.48	12.63	13.92	13.91	13.83	14.45	14.29	14.46	13.86	14.33	14.42	14.05
4	295.25	9.13	9.62	11.76	11.73	11.59	12.39	12.21	12.46	11.55	12.20	12.30	11.81
5	482.80	5.77	6.77	9.52	9.44	9.24	10.13	10.05	10.44	9.27	9.82	10.05	9.50
6	754.60	3.06	4.49	7.21	7.12	6.81	7.56	7.96	8.13	6.74	7.42	7.84	7.17
7	1130.65	1.39	2.82	5.28	5.18	4.75	5.14	5.50	5.77	4.37	4.91	5.50	4.68
8	1622.40	0.49	1.55	3.63	3.22	2.89	2.72	3.56	3.70	2.37	2.81	3.42	2.88
9	2228.35	0.17	0.68	2.30	1.66	1.46	0.68	1.95	2.03	0.93	1.13	1.86	1.89
10	2934.75	0.08	0.38	1.62	1.04	0.89	-0.01	1.13	1.19	0.19	0.32	0.93	1.38
11	3720.90	0.02	0.24	1.25	0.77	0.65	-0.26	0.83	0.88	-0.11	-0.01	0.45	0.89
12	4565.55	0.01	0.23	1.19	0.71	0.60	-0.33	0.74	0.79	-0.22	-0.11	0.28	0.74

TABLE 3b. Globally averaged salinity profiles simulated in Experiments I–XII, as well as the corresponding profile interpolated from the annually and globally averaged Levitus (1982) climatology.

Depth (m)	S (obs) (psu)	S (psu)											
		I	II	III	IV	V	VI	VII	VIII	IX	X	XI	XII
1	25.45	34.80	34.80	34.80	34.84	34.84	34.84	34.73	34.73	34.73	34.75	34.78	34.78
2	85.10	34.72	34.71	34.85	34.93	34.92	34.94	34.82	34.83	34.84	34.90	34.91	34.92
3	169.50	34.59	34.58	34.77	34.89	34.88	34.92	34.80	34.81	34.78	34.89	34.90	34.91
4	295.25	34.43	34.43	34.65	34.79	34.78	34.81	34.71	34.75	34.66	34.80	34.79	34.81
5	482.80	34.26	34.28	34.49	34.68	34.68	34.66	34.63	34.68	34.56	34.64	34.63	34.68
6	754.60	34.14	34.18	34.33	34.62	34.60	34.52	34.58	34.62	34.47	34.52	34.51	34.60
7	1130.65	34.09	34.13	34.23	34.63	34.60	34.50	34.58	34.61	34.48	34.47	34.44	34.61
8	1622.40	34.06	34.10	34.17	34.66	34.65	34.60	34.65	34.66	34.57	34.55	34.46	34.72
9	2228.35	34.05	34.08	34.13	34.70	34.69	34.69	34.68	34.69	34.67	34.62	34.49	34.77
10	2934.75	34.05	34.07	34.10	34.72	34.72	34.72	34.67	34.68	34.69	34.64	34.47	34.75
11	3720.90	34.05	34.07	34.09	34.73	34.73	34.74	34.67	34.68	34.71	34.65	34.47	34.72
12	4565.55	34.05	34.07	34.09	34.74	34.74	34.75	34.68	34.68	34.72	34.66	34.46	34.71

be necessary to resolve the observed salinity minimum found at intermediate depths. However, enhancing the Antarctic wintertime surface salinity tends to leave the simulated bottom water too cold, particularly when lateral mixing coefficients are low and NADW formation is weak (e.g., experiments VI, IX, and X).

To summarize the global-scale circulation simulated in each experiment, a table has been constructed showing several key features of the meridional overturning, as well as the modeled strength of the ACC. Table 4 shows the rate of overturning of AABW and NADW, as well as the rate of "outflow" of NADW, and the strength of the Drake Passage throughflow. Also included is the rate of overturning of a bottom water cell in the Southern Hemisphere (e.g., see Fig. 4c), defined as the maximum northward transport rate of bottom water south of the equator. The overturning rates of NADW and AABW are defined as the maximum transport rates in the North Atlantic and extreme Southern Ocean thermohaline cells, respectively (e.g., see Figs. 4, 13b). The magnitude of *NADW outflow* is defined as the rate of transport of *water of North Atlantic origin* across the latitude defining the southern tip of Africa (see, e.g., Fig. 13b). That is, the deeper outflow originating from Southern Ocean bottom water inflow is neglected in this statistic. So too is any upper-ocean outflow that has not been overturned in the North Atlantic (see, e.g., Fig. 14b).

The horizontal distribution of velocity has been checked extensively for zonal variability in the meridional flows defined in Table 4. This is necessary to ensure that the zonally integrated meridional overturning is not obscuring an inflow–outflow regime at a given depth. For example, a net meridional flow of 10 Sv out of the Atlantic basin could theoretically consist of 15 Sv ( $\text{Sv} \equiv 10^6 \text{ m}^3 \text{ s}^{-1}$ ) outflow of NADW adjacent to the coast of South America, and 5 Sv inflow of deep Southern Ocean water adjacent to the Cape of Good Hope. In the experiments described below, the respective transport values given in Table 4 genuinely represent the magnitude of NADW outflow, as well as the rate of northward flow of bottom water in the Southern Hemisphere. Errors arising from any zonal variability in flow directions are only of the order of 0.1 Sv.

In the following subsections we will present globally averaged and basin-averaged latitude–depth sections of simulated salinity. The distribution of temperature in the model ocean can be monitored with the profiles shown in Table 3a. To provide a climatological reference with which the salinity realizations can be compared, the long-term mean basin-averaged salinity sections from Levitus (1982) are presented in Fig. 2. At coarse resolution, we cannot hope to resolve some of the fine structure observed in the real ocean. However, we will ultimately isolate sufficient conditions for resolving the *global-scale* water masses of the World Ocean at coarse resolution.

TABLE 4. Meridional mass transport defining the overturning of Antarctic Bottom Water (AABW) and North Atlantic Deep Water (NADW) in each of the 12 experiments. Also included is the strength of the Southern Hemisphere (SH) bottom water cell centered at around 3500-m depth, as well as the rate of outflow of NADW into the Southern Ocean (defined in the text). The net mass transport of the Antarctic Circumpolar Current (ACC) is defined as the eastward transport through the Drake Passage. All values are given in Sverdrups ( $1 \text{ Sv} \equiv 10^6 \text{ m}^3 \text{ s}^{-1}$ ).

Experiment	AABW overturning	SH bottom water cell	NADW		ACC
			Overturning	Outflow	
I	31.1	31.1	—	—	—
II	22.2	11.7	—	—	57
III	28.1	10.2	—	—	125
IV	56.4	12.9	—	—	147
V	48.7	12.7	—	—	134
VI	47.4	17.4	—	—	145
VII (initial)	42.6	16.2	12.8	5.0	140
VII (final)	44.1	15.9	14.8	6.7	132
VIII	42.3	15.8	14.9	6.8	129
IX	42.7	14.4	13.7	5.5	136
X	41.8	13.7	14.0	7.4	151
XI (restoring)	11.5	19.3	18.4	8.6	155
XI (mixed)	18.3	22.8	18.6	8.6	189
XII	20.6	13.6	22.7	12.6	112

*a. Preliminary experiments (experiments I, II, III)*

The steady-state barotropic streamfunction in the first three experiments is presented in Fig. 3. Before evaluating the horizontal mass transport shown in these maps, it is worth examining the processes that can con-

tribute to a barotropic flow in the GFDL ocean GCM. By considering the equations for the external mode of velocity, it is apparent that there are only three ways to drive a barotropic flow in the modeled ocean. First, a nonlinear interaction between baroclinic modes of velocity can contribute to the barotropic mode. This

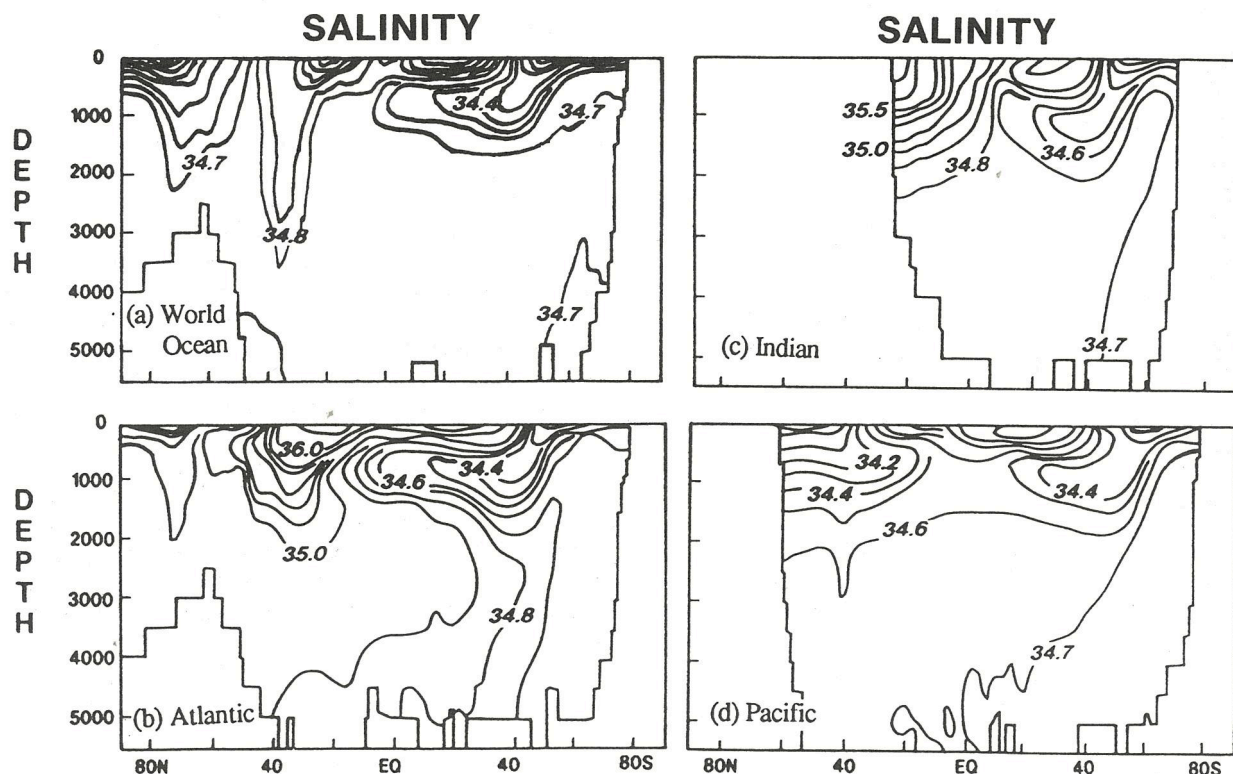


FIG. 2. Observed long-term mean globally and basin-averaged latitude-depth sections of salinity redrafted from Levitus (1982).

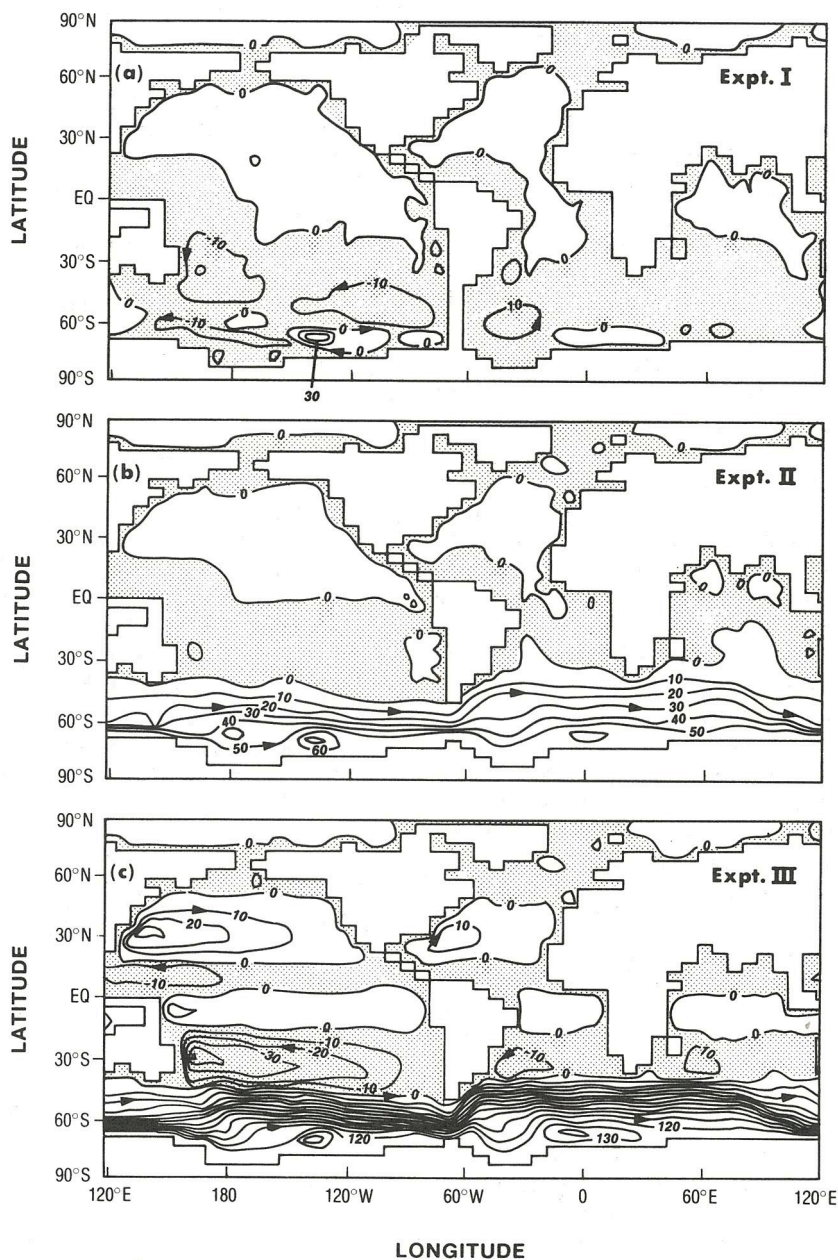


FIG. 3. Barotropic streamfunction in (a) experiment I, (b) experiment II, and (c) experiment III. Units are given in Sverdrups ( $1 \text{ Sv} = 10^6 \text{ m}^3 \text{ s}^{-1}$ ).

term is negligible in coarse-resolution models such as the one employed in the present study. Second, surface and bottom stresses can set up a barotropic flow. And thirdly, the so-called joint effect of baroclinicity and relief (JEBAR) can drive a barotropic circulation. JEBAR only contributes to the external mode of velocity in regions where there is a gradient in topography orthogonal to a gradient in density (Hsieh and Gill 1984). So, in a deep flat-bottomed coarse-resolution ocean GCM with only thermohaline forcing, the barotropic flow will be virtually zero everywhere at all times. In

the present study, it will primarily be the surface wind stress and JEBAR that drives the horizontal mass transport. On continental shelves, particularly near western boundary currents or in narrow channels, the bottom stress may also contribute significantly to the external mode.

In the thermohaline experiments (experiments I and II), any barotropic flow must originate from a coupling between a gradient in topography (such as a deep sill) and a gradient in density. With the Drake Passage closed in experiment I, the substantial deep zonal den-

sity gradients that do exist remain largely uncoupled with gradients in topography, and so the corresponding barotropic flow shows only weak small-scale circulations. The deep zonal density gradients referred to arise from differences between the abyssal water mass properties on either side of the Drake Passage sill. In spite of the highly idealized one-dimensional surface forcing in the thermohaline experiments, bottom water on the Atlantic side of the gap becomes somewhat colder than the corresponding bottom water on the Pacific side of the gap. Consequently, once the Drake Passage is opened (experiment II), a moderate ACC is established with 57 Sv flowing around Antarctica. Without any surface wind stress in this experiment, virtually all of this flow arises from the joint effect of baroclinicity and relief; that is, a deep zonal pressure difference across the Drake Passage sill (Gill and Bryan 1971). Away from the ACC region, the barotropic flow is virtually zero everywhere. By applying a surface wind stress in experiment III, the circumpolar current intensifies to 125 Sv, and the major subtropical gyre circulations are established (Fig. 3c). With the Indonesian Passage closed at this stage in the integrations, the East Australia Current (EAC) is too strong, and the Agulhas Current is far too weak. This is related to the role of the Indonesian throughflow in effectively transporting momentum from the Pacific wind stress field into the Indian Ocean via a Sverdrup flow (see section 4f).

An entirely different perspective on the oceanic circulation is given by the zonally integrated mass transport in the meridional plane, which is well defined as a global statistic, and in regions bounded by meridional barriers. The global meridional overturning in the preliminary experiments is shown in Fig. 4. While the barotropic flow appeared to have little structure in the closed Drake Passage experiment, the flow in the meridional plane shows a strong single-cell overturning adjacent to Antarctica. This corresponds with the formation of deep water in the first experiment; it is formed virtually exclusively in the extreme Southern Ocean. Because we employ *restoring* boundary conditions on both temperature and salinity in experiment I, the mode of deep water formation is very sensitive to the location of maximum surface-restoring density. This explains the strong preference for deep water to be formed adjacent to Antarctica in this experiment.

With the Drake Passage opened in experiment II, the global meridional overturning is entirely changed. The thermohaline component now displays two distinct deep circulation cells, one either side of the Drake Passage gap. The poleward flow in the subtropics now downwells north of the Drake Passage gap, with some flow continuing southward below the depth of the Drake Passage sill (Fig. 4b), but most recirculating in the tropical thermocline without being overturned adjacent to Antarctica. The thermohaline cell off Antarctica shows *reduced* deep downwelling of polar waters mostly recirculating in the ACC. In particular, only a

net 4.9 Sv outflows from the extreme Southern Ocean into the other ocean basins, which is within the range of estimates of AABW formation in the Weddell Sea (e.g., 2–5 Sv, Carmack and Foster 1975; 3–8 Sv, Weiss et al. 1979), though somewhat less than the estimated flux of bottom water out of the Ross Sea (13 Sv, Jacobs et al. 1985). The magnitude of the outflow of bottom water under the ACC (4.9 Sv) is not entirely represented by the map of meridional overturning in Fig. 4b. This is because there is a weak poleward flow of 0.8 Sv in the southeast Indian and southwest Pacific basins, compensating some of the bottom water outflow of 4.9 Sv. In some of the experiments, the *actual* outflow rate of AABW is substantially greater than the *apparent* outflow rate from a map of meridional overturning. When referring to rates of bottom water *outflow*, we refer to the actual equatorward volume transport of Ross Sea and Weddell Sea water, rather than the zonally integrated flow.

In experiment II, it is as though the existence of the Drake Passage gap has tended to prevent meridional flow across it. Gill and Bryan (1971) were the first to report a series of numerical experiments aimed at studying the sensitivity of the modeled circulation to the nature of the Drake Passage gap. They use a rectangular basin geometry and idealized surface forcing to demonstrate that upper-ocean poleward flow across

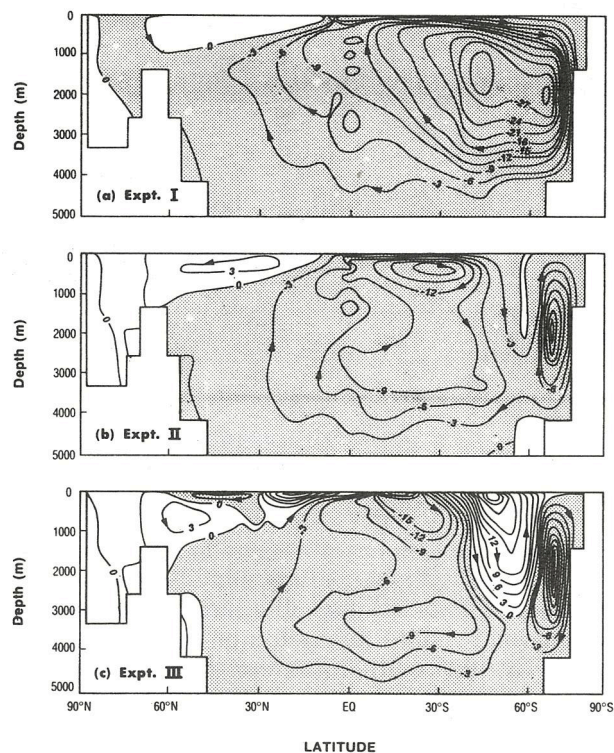


FIG. 4. Global meridional overturning streamfunction in (a) experiment I, (b) experiment II, and (c) experiment III. Transports are shown in Sverdrups.

the Drake Passage gap must be weak. This is related to a fundamental dynamical constraint unique to the Drake Passage: at the latitudes of the Drake Passage gap there are no north-south continental barriers to support a zonal pressure gradient. Without a zonal pressure gradient there can be no meridional geostrophic flow. Of course, there can be *ageostrophic* transport across the gap, but with the exception of wind-driven Ekman flows these are weak. Furthermore, below the *sill* of the Drake Passage, or at depths below the tops of midocean ridges spanning the latitude band of the Drake Passage, meridional barriers exist, and therefore geostrophic flows can be supported. These dynamical constraints are important in understanding the simulated meridional overturning in the present study (e.g., Fig. 4).

With a wind stress applied in experiment III, the meridional overturning becomes predominantly wind-driven near the sea surface. Poleward Ekman transport in the tropics and northward Ekman flow under the circumpolar westerlies obscures the previously clear component of thermohaline circulation in the model. In the deep ocean, the circulation remains largely unchanged, with bottom water flowing from the Southern Hemisphere into the Northern Hemisphere, eventually upwelling into the tropical thermocline. In the circumpolar region, the downwelling north of the Drake Passage gap has intensified dramatically due to the Ekman convergence in the subtropics. The upwelling in the ACC has also intensified, and with the northward Ekman flow under the polar westerlies, a closed circulation cell is apparent. This cell (recently termed the "Deacon cell") is characteristic of the circulation in the Southern Ocean in many recent World Ocean models (e.g., Bryan and Lewis 1979; Toggweiler et al. 1989; Semtner and Chervin 1988, 1991; Manabe et al. 1991). However, its shape and intensity appear to be sensitive to model resolution (Semtner and Chervin 1991), as well as the location of the maximum westerly wind belt relative to the Drake Passage gap (see section 4c). These circulation features are related to the previously discussed dynamical constraints governing meridional flow across the Drake Passage gap.

Globally averaged latitude-depth sections of temperature and salinity in the preliminary experiments are shown in Figs. 5 and 6. In spite of the dramatic differences in circulation realized in the first three experiments (both in the horizontal and vertical sense), the water-mass structure remains essentially the same. In all three preliminary experiments, both temperature and salinity decrease monotonically in the main thermocline. However, examination of the globally averaged *T-S* profiles listed in Table 3 shows that the simulated deep and bottom water is somewhat different between the experiments.

The deep water mass structure in the preliminary experiments can be readily explained in terms of the meridional overturning maps discussed earlier. In the

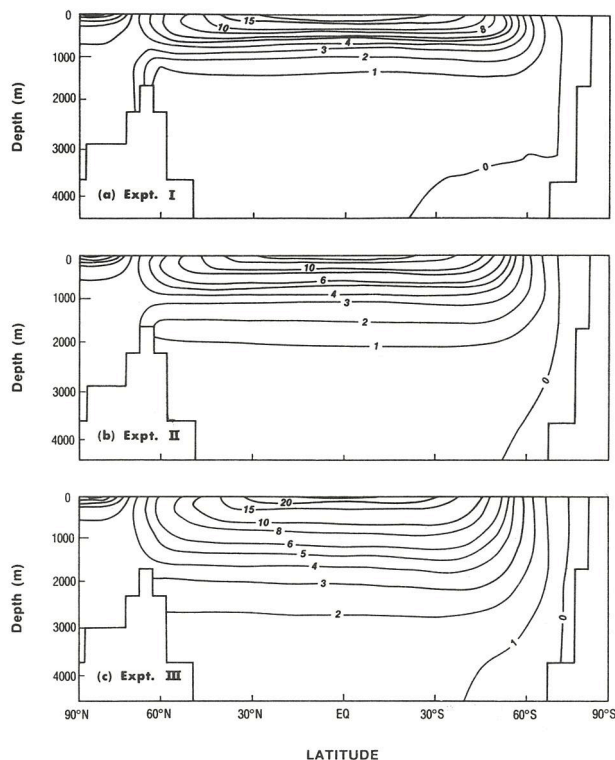


FIG. 5. Globally averaged latitude-depth sections of potential temperature (degrees Celsius) in (a) experiment I, (b) experiment II, and (c) experiment III. Contours are drawn at 1°C intervals for temperatures less than 5°C. Otherwise contours are drawn at 6°, 8°, 10°, 15°, 20°, and 25°C.

closed Drake Passage experiment, deep-water formation is found exclusively adjacent to Antarctica. At this stage in the experiments, there is no salinity adjustment of Antarctic shelf water. Consequently, the extreme Southern Ocean is cold (less than 0°C) and fresh (about 34.00 psu), and correspondingly, so too is the simulated deep water. The very weak vertical stratification in the bottom layers is related to the absence of any deep overturning of warm saline midlatitude water. When the Drake Passage is opened (experiment II), the meridional overturning is greatly changed, with deep downwelling of midlatitude water north of the Drake Passage gap. Furthermore, the (weaker) thermohaline overturning cell adjacent to Antarctica is now mostly isolated from the rest of the World Ocean, with only 4.9 Sv outflow of bottom water under the ACC. This serves to enhance the warmth, salinity, and vertical stratification of the simulated deep water. When applying a surface wind stress (experiment III), these processes are intensified; the midlatitude downwelling becomes very strong (Fig. 4), and the outflow from the Antarctic cell weakens further. Also, the wind stress drives a pair of overturning cells in the subtropics, weakening vertical temperature gradients in the main thermocline.

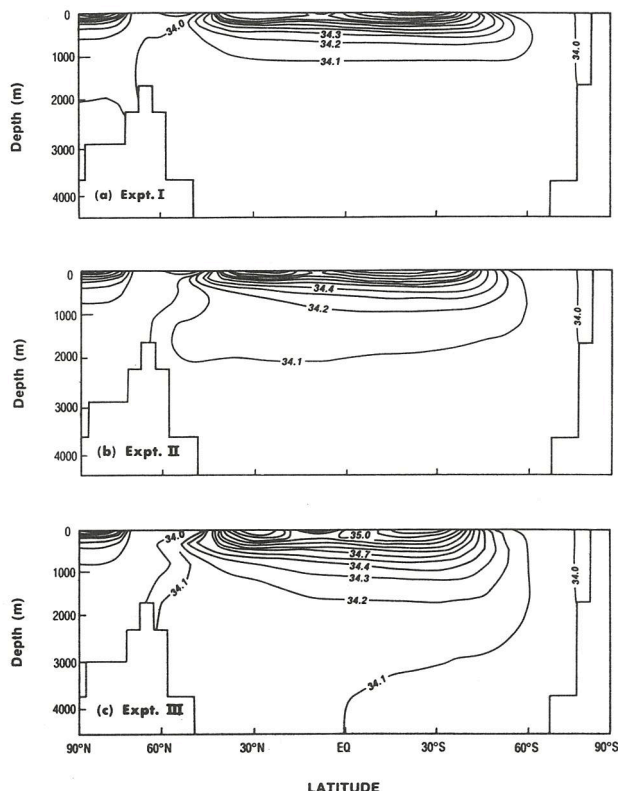


FIG. 6. Globally averaged latitude–depth sections of salinity (parts per thousand) in (a) experiment I, (b) experiment II, and (c) experiment III. Contours are drawn at intervals of 0.1 psu in the range 34.0–35.0 psu, otherwise a contour interval of 0.2 psu is adopted.

The northward heat transport in the preliminary experiments is presented in Fig. 7. To provide a climatological reference with which these distributions can be compared, some estimates of the total annual ocean heat transport are presented in Fig. 8. Northward heat transport in the preliminary experiments is dominated by a strong flux of heat toward the Southern Hemisphere, whereas observational studies suggest only weak interhemispheric asymmetry. This is related to the overturning component of the ocean general circulation in the preliminary experiments, which is dominated by sinking in the Southern Ocean (Fig. 4). The relatively weak response of the poleward heat transport to an open Drake Passage is a little surprising in view of the adjustments in the meridional overturning. By opening the Drake Passage, the advective transport of heat across the ACC is significantly weaker than when a continuous poleward surface flow existed (Fig. 4). However, there is a compensating increase in poleward heat diffusion in the newly established circumpolar current, due to an increased deep temperature structure in the open Drake Passage case.

In experiment III the addition of a surface wind stress strongly alters the northward heat transport. For example, the surface wind stress acts to *decouple* the two hemispheres in terms of meridional overturning (Fig. 4c). Correspondingly, the net transport of heat from the Northern Hemisphere to the Southern Hemisphere decreases substantially; in experiment II there is southward heat transport as far north as 16°N, whereas in experiment III it only extends as far as 5°N.

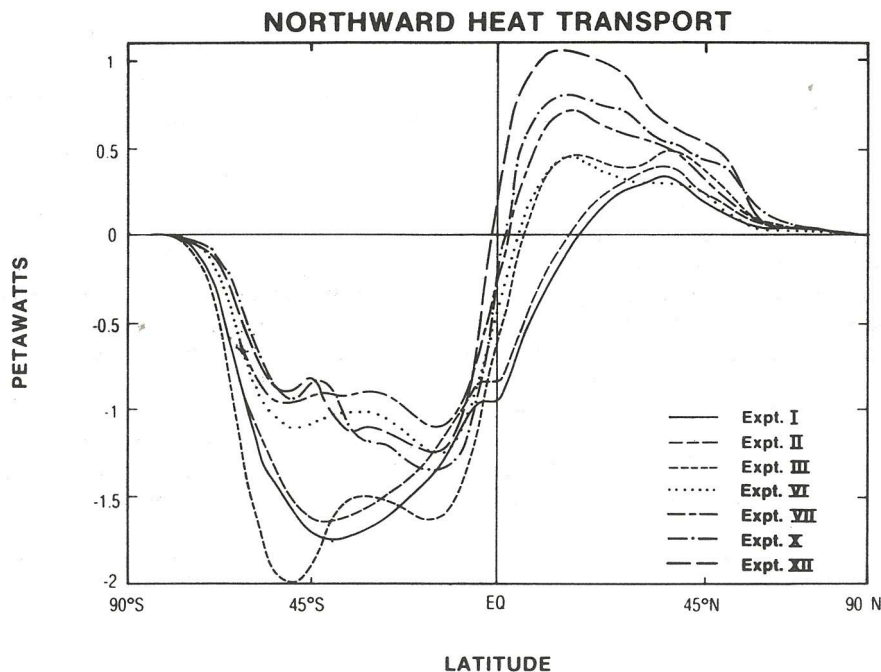


FIG. 7. Globally integrated northward oceanic heat transport in the preliminary experiments and in experiments VI, VII, X, and XII. Values are given in petawatts ( $1 \text{ PW} = 10^{15} \text{ W}$ ).

# TOTAL ANNUAL OCEAN HEAT TRANSPORT OBSERVED ESTIMATES

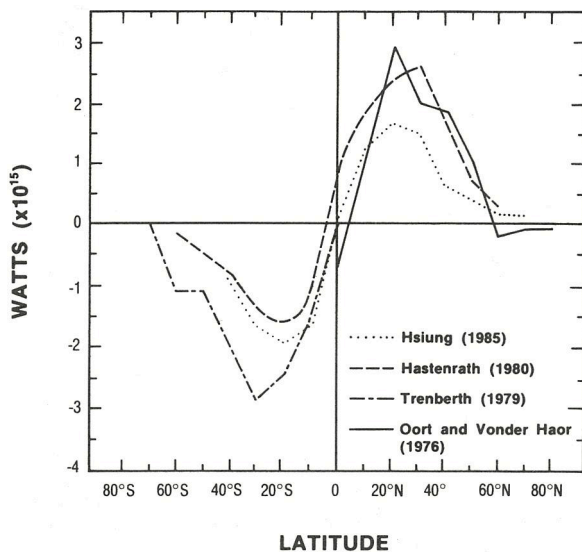


FIG. 8. Observed estimates of total annual northward ocean heat transport (PW) from Hsiung (1985), Hastenrath (1980), Trenberth (1979), and Oort and Vonder Haar (1976).

## *b. Enhanced Antarctic Bottom Water experiment (experiment IV)*

By the end of the preliminary experiments, the most erroneous aspect of the simulated  $T$ - $S$  distribution appears in the deep salinity field (Table 3). The long-term climatological data suggest a bottom water salinity of the order of 34.73 psu. In experiment III, a global mean salinity of only 34.09 psu is realized at the bottom level. Furthermore, no subsurface minimum in the salinity field is reproduced at intermediate levels. In the real World Ocean, both NADW and AABW enhance the salt content of the deep ocean. As we described in section 3, experiment IV investigates the response of the model to the establishment of genuinely salty AABW formation.

The globally averaged meridional overturning and salinity sections of experiment IV are presented in Fig. 9. With the inclusion of a more saline surface layer in the Ross and Weddell seas, the thermohaline overturning adjacent to Antarctica intensifies from 32 Sv (experiment III) to 56 Sv, which is likely to be too strong. Correspondingly, the outflow of bottom water under the ACC is strengthened (Fig. 9a), leaving the bottom and deep water marginally too cold. However, bottom water salinities become very realistic (Table 3b), and the pronounced salinity minimum of the North Pacific is reproduced (though at this stage in the experiments it appears in both the North Pacific and North Atlantic basins). In the Southern Hemisphere, the first signs of low salinity AAIW formation appear

at 60°S. However, the extent of its equatorward spreading is too weak, probably because of the high levels of horizontal diffusion present in these early experiments (e.g., see section 4d).

A series of two thermohaline experiments were also investigated with an enhanced salinity field in the extreme Southern Ocean. These two experiments correspond in every other way to experiments I and II described earlier. That is, the first experiment has a closed Drake Passage, while the second has a thermohaline-driven circumpolar current. The essential features of experiments I and II are retained, although the Antarctic circulation cells are intensified by the enhanced surface densities (as in experiment IV), as is the strength of the Drake Passage throughflow. Bottom water salinities are also increased, while deep-water temperatures cool because of the intensified overturning of cold Antarctic waters. A less predictable result involves the existence of the intermediate salinity minimum in these two runs. In the Drake Passage closed case, the equivalent of AAIW appears on the Pacific side of the Drake Passage gap, just to the north of the closed channel. It is formed by convective overturn and downwelling of fresh surface water at the eastern boundary. The low-salinity tongue spreads westward and equatorward from the formation region. Curiously, this is a robust feature in the remaining experiments that capture AAIW formation (England et al. 1993). Indeed, in the Drake Passage open case, the convective overturn and downwelling of relatively fresh water persists adjacent to the coast of southern Chile. In addition, a region of low salinity intermediate water formation appears in the Atlantic basin just north of the

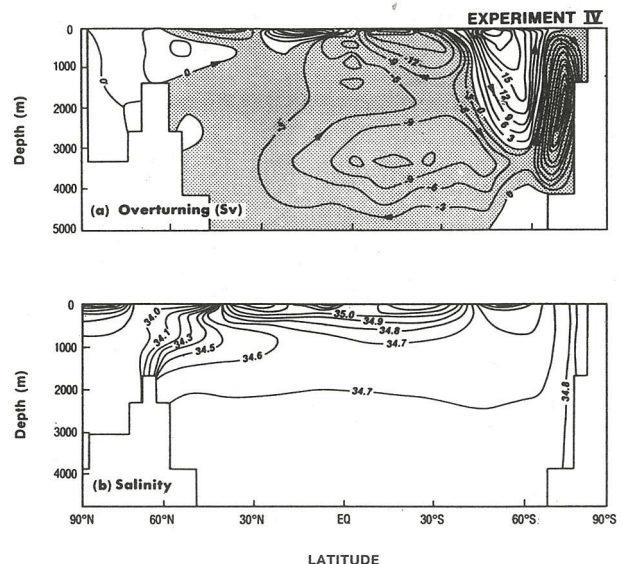


FIG. 9. Globally averaged (a) meridional overturning and (b) latitude-depth section of salinity in experiment IV. Units are given in (a) Sverdrups and (b) parts per thousand. The contour intervals correspond with those adopted for the preliminary experiments.

Drake Passage outflow. Again, this region of AAIW renewal remains apparent in the more sophisticated versions of the model (England et al. 1993).

Increasing the salinity of Antarctic surface water strengthens the intensity of the Southern Ocean thermohaline cell, but its effect on the northward heat transport is relatively small (Figure not shown). This is because the Antarctic cell remains rather isolated from the rest of the World Ocean due to the presence of the Drake Passage gap. With only weak geostrophic flow possible across the barrier-free zone, strengthening (or weakening) the formation rate of AABW has negligible effect on the upper-ocean meridional flow across the ACC.

### c. Narrow Drake Passage experiment (experiment V)

Having obtained an intermediate salinity minimum in experiment IV, it is apparent that the simulation of "NPIW" (appearing in both the Pacific and Atlantic basins) is far superior to the weak traces of AAIW that appear. Interestingly, in the thermohaline version of experiment IV previously discussed (i.e., no surface wind stress, Drake Passage opened, salinity enhanced off Antarctica) the equatorward spreading of AAIW matches its Northern Hemisphere counterpart. From this, it would seem that somehow the wind-driven circulation erodes the equatorward propagation of AAIW. The obvious candidate is the intense downwelling component of the Deacon cell, since this appears to advect straight through the region of low salinity intermediate water (Fig. 9).

In a recent study (England 1992a), we discussed the meridional overturning in experiments III, IV, and V (though they were denoted III, IIIa, and IIIb, respectively). In these maps, we included a contour representing the real and modeled Drake Passage bathymetry. To resolve the ACC in the model, the Drake Passage needs to be artificially wide (at least two velocity grid points are needed to simulate a realistic throughflow). However, by making it wide, and in particular, by extending the gap into the latitudes of strong westerly winds, the model tends to exaggerate the presence of the Deacon cell. In experiment V, with only a moderate change in the Drake Passage bathymetry, the Deacon cell becomes significantly weaker at intermediate levels (Fig. 10a). This is because there is now a more realistic meridional barrier to allow shallow geostrophic return flow under the surface Ekman drift.

The corresponding globally averaged salinity section in experiment V is included in Fig. 10. With a weakening of the intermediate downwelling component of the Deacon cell, there is a stronger equatorward spreading of the low salinity AAIW tongue. Closing off one grid point in the Drake Passage only moderately weakens the throughflow; in particular, the strength of the ACC decreases from 147 Sv (experiment IV) to

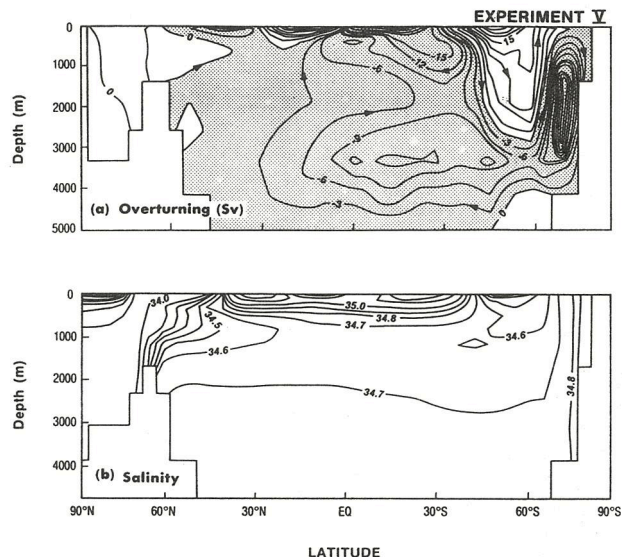


FIG. 10. Globally averaged (a) meridional overturning and (b) latitude-depth section of salinity in experiment V. Units and contour intervals are identical to Fig. 9.

134 Sv. Correspondingly, there is moderately less isolation of the extreme Southern Ocean by the circumpolar current, and hence the deep layers cool (Table 3a). Another way of viewing this is that narrowing the Drake Passage weakens the intensity of deep downward advection of warm midlatitude waters.

### d. Low horizontal diffusion experiment (experiment VI)

Until now, we have taken advantage of relatively high horizontal diffusivities in monitoring the global-scale response to a series of fundamental changes in the model geometry and boundary conditions. While high horizontal diffusion rates are advantageous in terms of model stability and convergence rates, they have a tendency to diffuse out any sharp frontal features in the surface density field. This makes it more difficult for the model ocean to form water masses that originate from frontal zones, such as AAIW and NPIW. It also weakens the model's capacity to transport near-surface water mass properties into the ocean interior. In regions of steeply sloping isopycnal surfaces (such as the Southern Ocean), high lateral diffusion rates can imply very strong and unrealistic diapycnal mixing of  $T-S$ , leading to excessive meridional heat transport across the ACC. In experiment VI, the level of lateral diffusion is scaled down significantly (as described in section 3), and therefore we can expect significant adjustments in the model's water mass configuration and ocean circulation.

The global mean meridional overturning and latitude-depth section of salinity in experiment VI are presented in Fig. 11. While the decreased rate of hor-

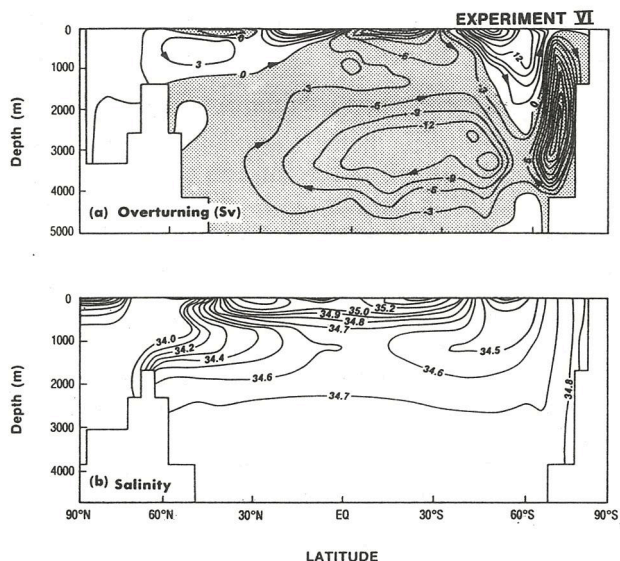


FIG. 11. Globally averaged (a) meridional overturning and (b) latitude-depth section of salinity in experiment VI. Units and contour intervals are identical to Fig. 9.

zontal diffusion in experiment VI has little effect on the Antarctic thermohaline cell (Table 4), the surface water mass properties are not diffused as much along their path of travel, and so more cold saline water is convected into the bottom layers of the model (Table 3). With denser bottom water being formed off Antarctica, the northward flow of deep water in the Southern Hemisphere is enhanced by almost 5 Sv (Table 4).

A map of differenced meridional overturning between experiments V and VI (not shown) reveals a dramatic change in the intensity of the Deacon cell with depth. While the upper-ocean wind-driven flow remains unchanged with lower horizontal diffusion, the intensity of downwelling at intermediate levels decreases substantially. This can be understood in terms of the approximate balance between horizontal diffusion and vertical advection in GCMs with high levels of lateral diffusion. For example, at about 900-m depth, the downward vertical mass flux between 30°S and 50°S decreases by as much as 12 Sv with lower rates of horizontal diffusion. This finding highlights the sensitivity of coarse-resolution ocean models to parameterized horizontal mixing.

Because of the decreased vertical advection and horizontal diffusion through the intermediate levels of the Southern Ocean, the representation of the model's AAIW improves significantly. In particular, the equatorward spreading of NPIW and AAIW is quite symmetric, as in the Levitus climatology (e.g., Fig. 2). The intermediate water is still marginally too saline because the year-round enhancement of Antarctic surface salinities puts too much salt into the deep and intermediate waters of the model. In a sense, it is surprising that AAIW appears in a multilevel model without any

parameterized isopycnal mixing, since it has long been believed that AAIW formation depends on along-isopycnal mixing and subduction of a mixture of Antarctic Surface Water and Subantarctic Upper Water (e.g., Sverdrup et al. 1942). From the results of the present experiment, it would seem that the formation of AAIW in ocean GCMs is essentially dependent on the large-scale advection and convective overturn of Subantarctic Waters. This has been detailed further in another report (England et al. 1993).

Because salinity has a smaller effect on density than temperature at midlatitudes, it should provide a better tracer of ocean circulation. While this is obviously the case with the model's "NPIW" (Fig. 11), the globally averaged AAIW low-salinity tongue is actually *orthogonal* to streamlines of zonally integrated meridional overturning. This is quite unlike the findings of some other World Ocean GCMs that capture an Antarctic salinity minimum. For example, both the eddy-resolving calculations of Semtner and Chervin (1988, 1992) and the pioneering World Ocean model of Bryan and Lewis (1979) show tongues of AAIW matched by zonally integrated northward flows in the intermediate layers.

Because we are comparing two globally averaged statistics (i.e., the Deacon cell and the zonally averaged salinity section), we may be overlooking much zonal variability in both salinity and vertical motion. To clarify the relative distributions of vertical motion and AAIW in experiment V, comparative horizontal sections of vertical velocity and intermediate salinity were presented and discussed in an earlier report (England 1992a). These maps elucidate the mutual existence of the Deacon cell and the low-salinity AAIW tongue in experiment V. For example, notably strong downwelling is apparent on either side of the southern tip of South America, corresponding with the location of two distinct salinity minima. In spite of this, a more sophisticated study of the dynamics in the region (England et al. 1993) reveals that the convective overturn of Subantarctic Waters off Cape Horn is the principal mechanism to renew the model's intermediate water.

The distribution of Southern Hemisphere salinity at 1131-m depth (level 7 of the ocean model) in experiment VI is presented in Fig. 12. For comparison with observations, the long-term mean climatological map of salinity observed at 1000 m is also included. From a comparison between the observed and modeled maps of intermediate salinity, it appears that the model is representing the ocean's tendency to form fresh intermediate water off the coast of Southern Chile. In a detailed analysis of Southern Ocean hydrographic data, McCartney (1977) also isolates this region as the principal location of AAIW formation. Another observed salinity minimum appears in the confluence region of the Malvinas and Brazil currents (Fig. 12a), which is also believed to be a location of AAIW renewal

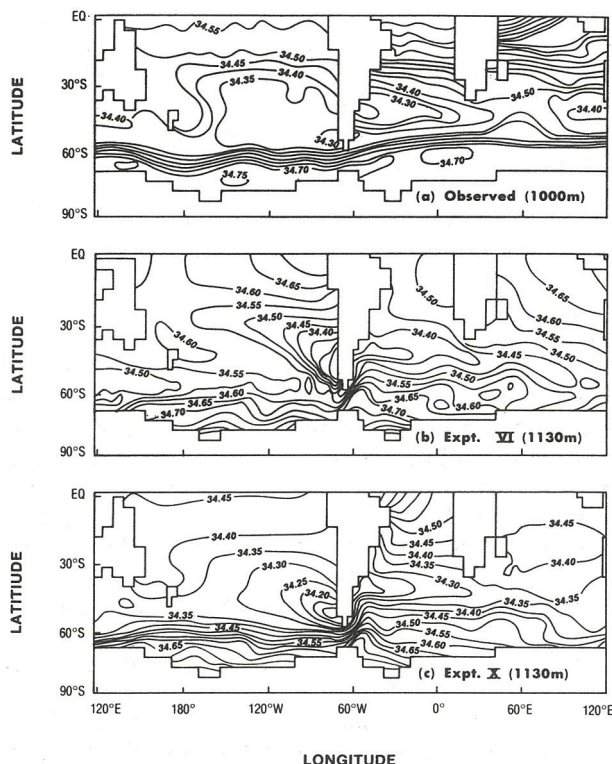


FIG. 12. (a) Observed long-term annual-mean salinity at 1000-m depth, redrafted from Levitus (1982). (b) and (c) Salinity at 1131-m depth (level 7 of the ocean model) in the low-diffusion experiment with *idealized* surface forcing (experiment VI) and in the isopycnal mixing experiment with *realistic* annual-mean surface forcing (experiment X).

(McCartney 1977). Again, the model handles this feature in the salinity distribution very well.

With a decrease in lateral diffusion rates in experiment VI, the poleward heat transport across the ACC (at 50°S) is almost halved from 2.05 PW (experiment V) to 1.13 PW (1 PW =  $1 \times 10^{15}$  W). The maximum southward heat transport now occurs at 13°S (previously it occurred at 50°S), which is more in line with estimates of observed poleward heat transport in the Southern Hemisphere (e.g., Fig. 8). The reason for the dramatic weakening of poleward heat transport in the Southern Ocean is not difficult to understand. The steeply sloping isotherms characterizing the Southern Ocean appear in the model realization of temperature in both the low and high diffusion experiments. As such, any parameterized horizontal eddy mixing will take place *across* isopycnal surfaces, strongly diffusing heat poleward. Decreasing the horizontal diffusion coefficients in experiment VI greatly reduces this spurious feature of the model.

An ancillary experiment was investigated with an even *higher* level of parameterized horizontal diffusion than in the preliminary experiments. The magnitude of  $A_{HH}$  in this experiment corresponds with the levels of lateral diffusion employed in certain ocean climate

models (e.g., Washington and Meehl 1989). The profile of  $A_{HH}$  again follows Eq. (2), only now  $A_{SH} = 1.0 \times 10^8 \text{ cm}^2 \text{ s}^{-1}$  and  $A_{BH} = 0.5 \times 10^8 \text{ cm}^2 \text{ s}^{-1}$ . That is, the profile of diffusion coefficients is an order of magnitude higher than in the low-diffusion experiment (experiment VI) and at least a factor of 2 greater than in the preliminary experiments (Table 2). Not surprisingly, the model simulation in this case becomes quite unrealistic. The downwelling component of the Deacon cell significantly deepens and intensifies, transporting more than 20 Sv of midlatitude water below 2500 m. Furthermore, the tropical overturning cells now ventilate the bottom layers of the model ocean, similar to what Manabe and Stouffer (1988) obtained in one of their experiments (England et al. 1992). With water of midlatitude origin sinking to great depths, the Antarctic thermohaline cell becomes completely isolated from the Deacon cell, with all of the water that sinks adjacent to Antarctica upwelling south of the Drake Passage gap. The spurious diapycnal mixing of temperature associated with the very high lateral diffusion rates increases the poleward heat transport across the ACC to 2.99 PW at 50°S. A similar spurious diffusion of heat can be seen in the Washington and Meehl (1989) climate model, indicating that their levels of lateral diffusion are too high. In their model ocean the excessive heat transport leaves the ocean too warm by as much as 8°C in the extreme Southern Ocean, largely prohibiting sea ice formation around the Antarctic continent.

#### e. North Atlantic Deep Water experiment (experiment VII)

Up until experiment VI, the thermohaline and momentum forcing of the surface layer has been constructed from simple one-dimensional fields derived from observations. There is only weak zonal variability in surface temperatures and salinities (e.g., in western boundary currents) because of the slight freedom of the model to deviate from the forcing conditions. In the Northern Hemisphere, both the North Pacific and North Atlantic surface salinities are too fresh to drive any deep thermohaline overturning (e.g., Fig. 11a). However, a major component of the ocean's thermohaline circulation involves the formation and recirculation of NADW (Gordon 1986), driven primarily by high surface salinities in the North Atlantic.

As a first attempt at capturing NADW, we differentiate between the relative freshness of the North Pacific and saltiness of the North Atlantic in a very simple way. Instead of referencing zonally averaged observations of *global* surface salinity, we restore toward *basinwide* zonal averages in these two regions. In every other respect, the initial stage of experiment VII is identical with experiment VI. With high sea surface salinities in the North Atlantic, a thermohaline overturning of warm salty NADW is established (Table 4).

However, while 12.8 Sv overturns at high latitudes, only 5.0 Sv flows out into the Southern Ocean. This outflow of NADW is somewhat weaker than observations suggest (e.g., 17 Sv, Roemmich and Wunsch 1985; 13.5 Sv, Gordon 1986; 20 Sv, Broecker 1991; 17 Sv, Rintoul 1991), though only slightly weaker than the outflow obtained in other World Ocean models (e.g., Toggweiler et al. 1989). Simulating a realistic interocean exchange of NADW is important if the model is to properly represent the global ocean circulation at its largest scale. Examination of water mass properties at this stage in experiment VII shows the bottom water to be too cold and saline, suggesting that the model is forming too much AABW. Obviously a year-round enhancement of the Antarctic surface salinities is quite unrealistic; it would be more appropriate to only enhance the wintertime values corresponding with the time of observed sea ice formation. In view of this, experiment VII is run out to steady state with high Antarctic surface salinities during only June, July, and August of each year. The resulting *annual-mean* meridional overturning and salinity fields are shown in Fig. 13. Because of the new zonal asymmetry in the model configuration, it is worth showing the Atlantic basin component of meridional overturning explicitly, as well as the zonal mean latitude–depth sections of salinity in each ocean basin.

Altering the consistency of Antarctic salinity enhancement enables the modeled bottom water to warm significantly (Table 3a). The *overturning* of NADW is only marginally increased from the earlier stage of experiment VII (up from 12.8 Sv to 14.8 Sv), but nearly all of the enhanced overturning flows out into the Southern Ocean (i.e., the *outflow* increases from 5.0 Sv to 6.7 Sv). This suggests that the interocean exchange of NADW is controlled to an extent by the density of AABW formed in the Southern Ocean. By decreasing the salt adjustment term, we allow the model's bottom water to become somewhat fresher and warmer, and hence not as dense. This allows an enhanced thermohaline exchange of NADW. Another way of viewing this is that the tendency for the thermohaline circulation to transport surface water southward (Figs. 4a,b) has been reduced by weakening the Antarctic salt adjustment. In turn, the effective (northward) inflow of NADW across the latitude of the Cape of Good Hope increases, and necessarily, so too does the eventual outflow (Table 4). Correspondingly, a tongue of high salinity water spreads from the North Atlantic into the Southern Ocean (Fig. 13c), although its southward penetration is marginally weaker than in the observational data (see Fig. 2).

Another pleasing aspect of experiment VII is the improved structure of the low salinity AAIW tongue. By only having a *wintertime* salinity adjustment, we get a realistic halocline in the immediate vicinity of Antarctica on an annual average. Previously, the isohalines in the extreme Southern Ocean were very steeply sloped

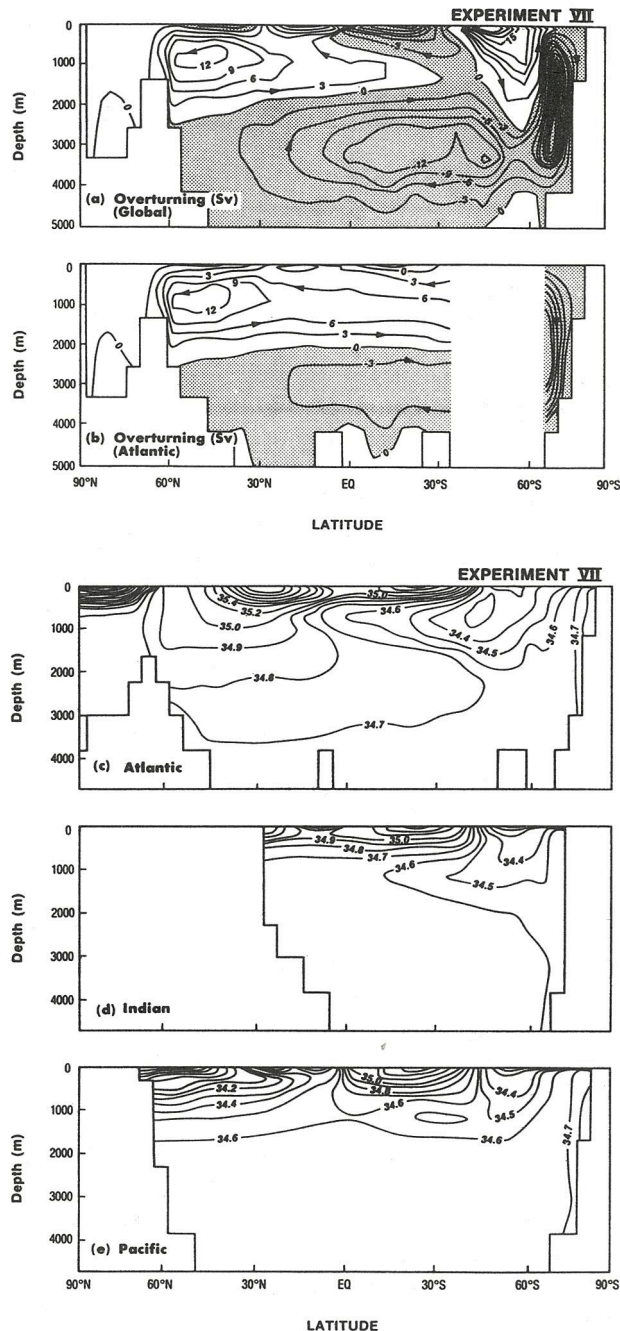


FIG. 13. Meridional transport streamfunction (Sv) for the (a) global and (b) Atlantic basin overturning in experiment VII. In (b) no streamfunction can be defined at latitudes where the ocean is free to exchange mass zonally. (c)–(e) Zonally averaged sections of salinity in the Atlantic, Indian, and Pacific basins of experiment VII. Contour intervals follow the convention established in the preliminary experiments.

up to the sea surface (Fig. 11b), with year-round deep vertical convection removing vertical gradients in temperature and salinity. In experiment VII, there is only *wintertime* deep convective adjustment through

the surface layer. The fragmented isohalines in the Pacific and Atlantic traces of AAIW suggest that not enough low-salinity water is being subducted into the intermediate layers of the model. We will see in section 4g that the inclusion of an isopycnal mixing scheme diffuses more low salinity water into the ocean interior, further improving the representation of intermediate water.

To study the thermohaline circulation of NADW, it is revealing to consider the path of outflow and inflow preferred by it and its source water. Some simplified global-scale thermohaline "conveyor belts" have been constructed to describe the process of NADW renewal (e.g., Gordon 1986; Broecker 1991), and these schemes can be readily evaluated within models of the World Ocean (e.g., Semtner and Chervin 1991). Even though the inclusion of NADW weakens the strength of the ACC past the southern tip of South Africa, the flow remains strictly *eastward* at all levels. That is, there is no direct Indian to Atlantic flow around the Cape of Good Hope. As such, the return path of NADW must be via the Drake Passage in the present experiment.

The inclusion of a Northern Hemisphere source of deep water correspondingly draws more heat northward (Fig. 7) because of the required replacement of North Atlantic surface water with water of low-latitude origin. As the warm saline low-latitude water is advected into the North Atlantic Ocean, the surface thermohaline forcing implies that the ocean releases heat and moisture into the atmosphere, in agreement with observed surface buoyancy fluxes in the region (e.g., Esbenson and Kushnir 1981; Wijffels et al. 1992). As heat and moisture are lost to the atmosphere, the surface layer densities increase, which in turn destabilizes the water column. This offsets deep convective overturn of the North Atlantic surface waters, forming deep mixed layers and ultimately renewing NADW.

#### *f. Open Indonesian Passage experiment (experiment VIII)*

There remains some debate as to whether the global-scale thermohaline circulation of NADW contributes a substantial component of the Indonesian throughflow (Gordon 1986) or whether the majority of NADW eventually returns to the Atlantic basin via the Drake Passage (Rintoul 1991). Up until experiment VII, the Indonesian Passage is completely blocked off, which keeps the Agulhas Current far too weak (order 15 Sv). Furthermore, as was mentioned above, there is no barotropic or baroclinic flow from the Indian Ocean into the Atlantic via an "Agulhas leakage" (i.e., a flow *westward* around the Cape of Good Hope), so that NADW must return via the Drake Passage. In experiment VIII, however, the Indonesian Passage is opened to a full throughflow, so that the return path of NADW can follow the conveyor belt of Gordon (1986).

When the present series of experiments were origi-

nally being formulated, it was thought that experiment VIII would provide a rather novel approach to understanding the role of the Indonesian throughflow in determining the circulation and water mass configuration of the World Ocean. In the meantime, however, a very detailed account of the response of a global ocean GCM to a variety of Indonesian throughflow configurations has been presented by Hirst and Godfrey (1993). It turns out that the adjustment of our model to a full Indonesian throughflow is very similar to an equivalent case presented in their study. As such, we will limit our discussion of experiment VIII somewhat, referring the interested reader to Hirst and Godfrey (1993).

The overall barotropic adjustment of the model to an open Indonesian Passage is similar to that expected under a simple Sverdrup model (e.g., Godfrey 1989). The net throughflow simulated is 22.4 Sv, which is stronger than recent estimates based on observations (10–13 Sv, Godfrey 1989) and Sverdrup model theory ( $16 \pm 4$  Sv, Godfrey 1989). The strong Indonesian throughflow is part wind-driven (16 Sv) and part driven by strong gradients in density across the Indonesian Passage sill (i.e., JEBAR; 6 Sv). In response to the depth-integrated flow from the Pacific to Indian Ocean, the East Australia Current weakens by 28 Sv, and the Agulhas Current strengthens by about the same amount. Under a pure Sverdrup regime, the Indonesian throughflow represents a transfer of South Pacific wind-driven flow (from the EAC) into the Indian Ocean South Equatorial Current, ultimately enhancing the Agulhas Current and outflow into the Atlantic basin (see, e.g., England et al. 1992). Correspondingly, in the Agulhas outflow region the eastward flow past the tip of South Africa weakens by up to 20 Sv, and there is now a weak Agulhas leakage of 0.5 Sv in the surface 1347 m (down to level 7).

Opening the Indonesian Passage clearly affects the interocean exchange of heat and fresh water in a World Ocean model (Hirst and Godfrey 1993). However, these strong internal adjustments do not appear in some of the global-scale diagnostics presented so far (e.g., Table 3, and poleward heat transport, figure not shown) partly because restoring boundary conditions limits the global-scale response of the model to some degree, but also due to the nature of the dynamics governing the throughflow. Being largely governed by a Sverdrup regime, opening the Indonesian Passage mainly serves to redistribute the barotropic flow, and little response is detected in the global meridional overturning.

#### *g. Isopycnal mixing experiment (experiment IX)*

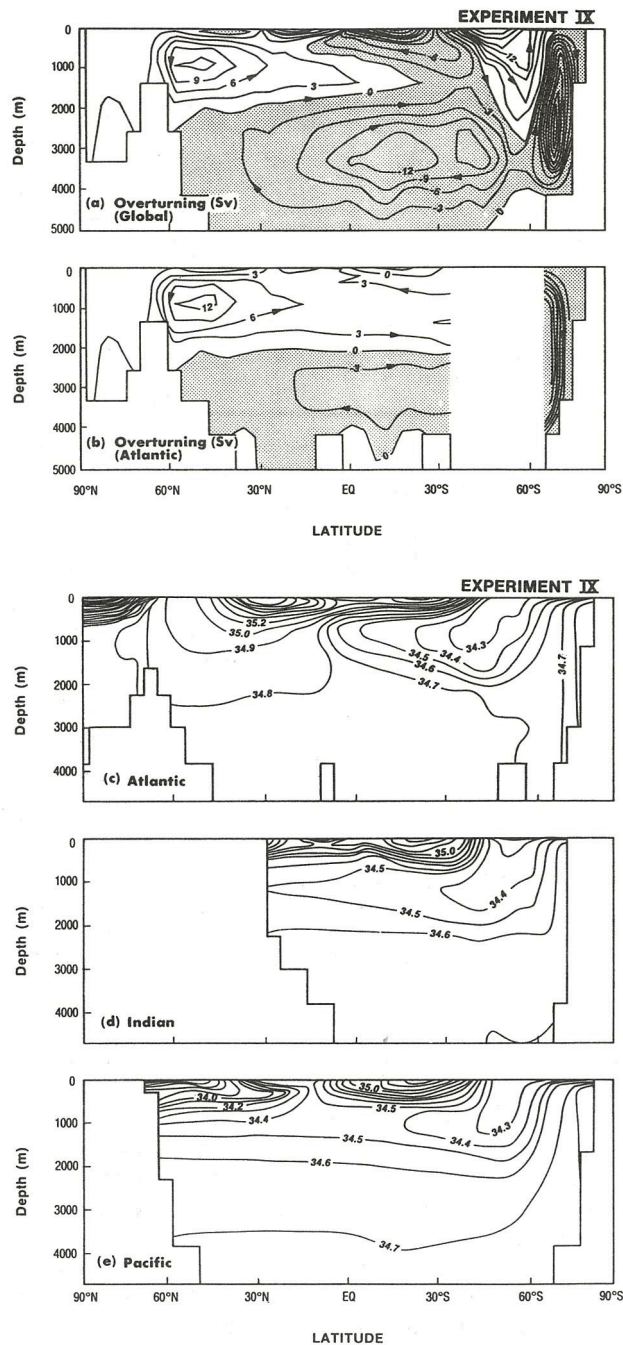
Scalar properties in the ocean are mixed rather efficiently by mesoscale eddies along surfaces of constant potential density (Wüst 1933). A chronic deficiency of coarse-resolution multilayer models is the required level of lateral diffusion to ensure numerical stability. High levels of lateral diffusion can imply spurious rates

of diapycnal mixing in regions of steeply sloping isopycnal surfaces (section 4d). Without going to higher resolution in the horizontal, we cannot substantially decrease the parameterized rate of geopotential mixing used in the low-diffusion runs (experiments VI–VIII); in the present isopycnal mixing experiment (experiment IX), only a 25% reduction in  $A_{HH}$  is realized at all depths (Table 2). However, we can at least enhance the parameterized rate of mixing along isopycnal surfaces using the scheme proposed by Redi (1982).

The globally averaged  $T$ – $S$  profiles of Table 3 reveal the large-scale World Ocean response to the inclusion of the isopycnal mixing scheme. For example, the model's bottom water becomes more cold and saline, whereas the intermediate water freshens substantially. The corresponding globally averaged and basin-averaged meridional overturning and salinity sections are shown in Fig. 14.

The enhanced deep salinities and colder bottom water originate from the Antarctic shelf in the isopycnal mixing experiment. Figure 15 compares the rate of change of salinity due to vertical diffusion (which includes a component of isopycnal diffusion in experiment IX) before and after an isopycnal mixing scheme has been adopted. Notice that the role of vertical diffusion is increased by at least two orders of magnitude south of  $30^{\circ}\text{S}$  once the slope of isopycnal surfaces is considered when determining diffusion rates, so that it in fact becomes as important as convection and advection in determining the model's water mass configuration in the Southern Ocean. Even though we still only increase the Antarctic surface salinities for three wintertime months, the steeply sloping isopycnal surfaces in the extreme Southern Ocean now provide an efficient path for mixing the saline wintertime surface water downward (denoted by the unstippled regions of Fig. 15b). Furthermore, the 25% reduction in  $A_{HH}$  enables less diapycnal diffusion of water masses as they are mixed and convected into the ocean. These two processes combined bring the bottom water mass characteristics ( $T = -0.22^{\circ}\text{C}$ ,  $S = 34.72$  psu) closer to the wintertime sea surface conditions off Antarctica ( $T = -1.08^{\circ}\text{C}$ ,  $S = 34.90$  psu).

The freshening of intermediate water in the isopycnal run is a very positive aspect for the model. It has long been thought that isopycnal mixing of water originating from the polar front is the means by which AAIW becomes subducted into the ocean interior (e.g., Sverdrup et al. 1942). By including an isopycnal mixing scheme, more of the fresh surface water in the polar front becomes mixed into the model's intermediate levels (Figs. 14c–e, 15b). Comparing a horizontal section of intermediate salinity in this experiment (not shown) with observation (Fig. 12a) shows that the model's intermediate water is still principally renewed off the coast of Southern Chile and in the Malvinas–Brazil confluence region. However, a more detailed analysis of the salt balance in the AAIW tongue shows a substantial



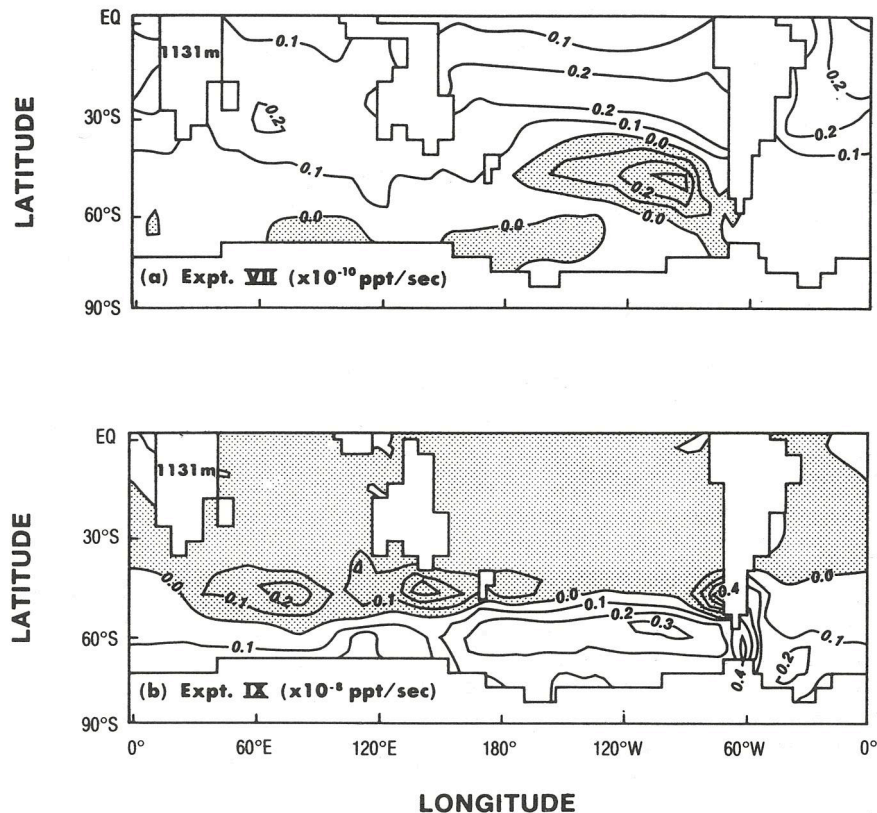


FIG. 15. The time rate of change of salinity due to vertical diffusion at 1131 m depth in (a) experiment VII (without isopycnal diffusion) and (b) experiment IX (with isopycnal diffusion). Stippled areas indicate that the vertical diffusion term is freshening the intermediate waters. Notice in particular the different scales used in each panel; changes in salinity due to vertical diffusion south of 30°S are at least two orders of magnitude higher with an isopycnal mixing scheme.

Figs. 14a and 13a). There is a slight weakening (order 1 Sv) of the rate of overturning and outflow of NADW (Table 4), primarily because some of the intermediate level inflow into the Atlantic basin returns to the Southern Ocean without being overturned in the North Atlantic (Fig. 14b). The relative robustness of the Deacon cell to the inclusion of an isopycnal mixing scheme could be in part due to the background lateral diffusion, which is only reduced by 25% in the present experiment. Because the meridional overturning remains relatively unchanged when an isopycnal mixing scheme is adopted, the adjustments in poleward heat transport are minor (Fig. not shown). For example, in the North Atlantic there is a slightly weaker thermohaline overturning in the isopycnal run, and correspondingly, the northward heat transport is reduced marginally.

#### *h. Realistic annual forcing experiment (experiment X)*

The zonal variability of surface conditions in the major ocean basins of the World Ocean is substantially

weaker than meridional variations, particularly in the surface temperature and wind stress fields. Up until now, our experiments have been configured in recognition of this feature, with *idealized* basin-averaged surface conditions forcing the ocean model. In experiment X, however, we upgrade the surface forcing in the isopycnal mixing experiment to include the full zonal variability of surface wind stress and thermohaline conditions (as described in section 3). The wind-stress forcing follows the annual mean climatology of Hellerman and Rosenstein (1983), which happens to be generally stronger than the idealized one-dimensional forcing used thus far. The Antarctic salt adjustment term is maintained during June to August of each year, though in view of the increased production of cold saline AABW simulated under isopycnal mixing conditions, we have confined the adjustment to be somewhat closer to Antarctica (section 3).

The largest-scale response of the model in experiment X shows a warming and freshening of the bottom water (Table 3), primarily because the salt adjustment term has been reduced. The permanent thermocline deepens and becomes more diffuse in response to the

stronger tropical wind-driven overturning. The stronger tropical overturning also enhances the poleward heat transport at low latitudes (Fig. 7). The higher (and more realistic) thermocline salinities are due to the enhanced Ekman pumping of highly saline subtropical waters. Previously, there was no distinction between the relatively fresh western and eastern boundary salinities and the more saline midbasin water (e.g., see Levitus 1982).

The thermohaline overturning of NADW only increases marginally (from 13.7 Sv to 14.0 Sv) when the full Levitus  $T$ - $S$  forcing is adopted. However, more of the overturned water flows southward at deep levels, so that the NADW outflow increases by almost 2 Sv (Table 4). At first it was thought that the decreased production rate of cold saline AABW had enabled an increased outflow of NADW into the Southern Ocean, similar to the process described in section 4e. However, another factor to be considered in experiment X is the different wind-stress forcing at the ocean surface. As was mentioned earlier, the Hellerman and Rosenstein (1983) wind-stress forcing is generally stronger than the idealized one-dimensional fields used previously. As such, the northward surface flow under the polar westerlies increases (by 2.5 Sv), and by continuity of mass, we can expect an increased return flow at deeper levels. Recently, Toggweiler and Samuels (1992) have correlated the simulated outflow rate of NADW with the strength of Southern Ocean winds, using the results of several numerical experiments of varying configurations. They go on to suggest the possibility of a very simple relationship between the magnitude of deep outflow from the Atlantic Ocean and the magnitude of northward wind drift across the northern edge of the Drake Passage gap.

Except for the changes mentioned above, the overall picture of ocean circulation and water mass formation in experiment X remains quite similar to the simulation detailed in the preceding model run. For this reason, the global maps of meridional overturning and water mass configuration are not presented for experiment X. One disappointing aspect of the present simulation is that in spite of a weakening of AABW production, as well as a corresponding increase in NADW outflow, the model bottom water remains too cold by about  $1^{\circ}\text{C}$  (Table 3a). Furthermore, it was hoped that the weakened salt source adjacent to Antarctica would be compensated by an enhanced overturning and outflow of saline NADW. In experiment X, however, the deep ocean salinity decreases in each ocean basin, even in the far North Atlantic.

Some ancillary experiments were investigated to consider several processes that might enhance the production rate and outflow of NADW. In one case, the Mediterranean Sea was included in the model domain (section 2), resulting in an outflow of saline Mediterranean water at intermediate depths. However, the rate of NADW production and outflow only increases by

about 0.5 Sv. The corresponding water mass configurations are hardly affected on a global scale. In another experiment, the deep and intermediate vertical diffusivities were increased globally in view of some recent findings by Cummins (1991). In an idealized single-basin experiment, Cummins (1991) finds that higher vertical diffusivities in the deep ocean result in an enhanced deep thermohaline overturning and vertical stratification. In the present model, increasing deep vertical diffusion coefficients globally has little effect on the maximum overturning rate of deep-water formation. However, the interocean exchange is somewhat stronger in both the Atlantic and Antarctic regions. Differenced circulation maps (not shown) reveal that AABW outflow intensifies by about 12 Sv, and NADW outflow by 2.5 Sv. That is, the overall response of the model to higher deep vertical diffusion is to produce even more cold saline bottom water off Antarctica.

The developing success of the model at capturing AAIW formation has been demonstrated in the series of latitude-depth salinity sections presented so far. At this stage it is worth revisiting the *horizontal* map of salinity at depth 1131 m originally presented for experiment VI. Figure 12 includes the corresponding level map of annually averaged salinity in experiment X. The salinity map can be compared directly with the same figure for experiment VI, and the climatological distribution of Levitus (1982). In retrospect, it is a little surprising that the zonal variability of AAIW was reasonably well reproduced in experiment VI, in spite of the one-dimensional nature of the surface forcing conditions employed. This suggests that the location of ocean boundaries is critical to the location of AAIW renewal, because the only zonal variability in the configuration of experiment VI is the variation in bottom bathymetry and continental outlines. This has been detailed further by England et al. (1993). For now, it is worth noting that by experiment X the AAIW salinities have become realistically fresh (due to the isopycnal mixing scheme), and the location of the two major intermediate minima are reproduced. These relative minima (off Southern Chile and in the Malvinas-Brazil confluence) have been a robust feature of the model even in very idealized thermohaline cases (section 4b). However, the inclusion of an isopycnal mixing scheme was required to freshen the intermediate water at certain locations (Fig. 15b).

#### *i. Cutoff AABW enhancement experiment (experiment XI)*

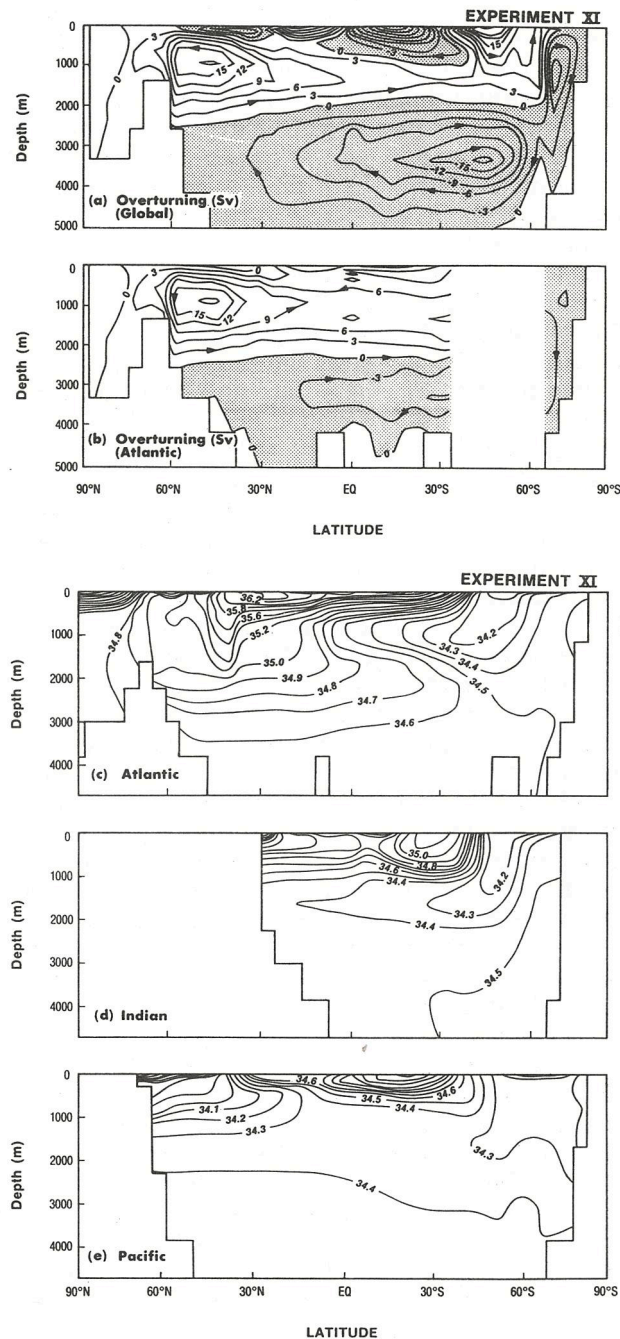
In view of the anomalously cold bottom water formed in an isopycnal model when Antarctic surface salinities are enhanced (Table 3a), it is worth reconfiguring experiment X without any Antarctic salt adjustment. This would also enable a more direct comparison between the present study and some other World Ocean models run with unadjusted annual

mean surface conditions (e.g., Toggweiler et al. 1989). The inclusion of the Mediterranean Sea in an ancillary version of experiment X is maintained in experiment XI. The first version of this experiment is run with *restoring* boundary conditions on both  $T$  and  $S$ , and is integrated out to a steady-state solution.

The global and basinwide meridional overturning and salinity configuration in experiment XI are presented in Fig. 16. Removing the salt adjustment term alters the modeled overturning in most regions of the ocean. The intense vertical motion in the Antarctic thermohaline cell is replaced by a weaker overturning of 11.5 Sv. In spite of this, the weaker Antarctic cell flows into an intensified deep thermohaline cell centered at 45°S (Table 4). The upper branch of this cell is driven by both the outflow of deep water in the Atlantic basin, as well as the return flow of bottom water originating from the Southern Ocean (Fig. 16b). The lower branch of the cell signifies the northward flow of bottom water originating from the Ross and Weddell seas (England 1992b). The intensification of this deep circulation in spite of a decreased overturning of AABW is quite surprising and it serves to highlight the isolation of the extreme Antarctic waters in determining global flows. The prognostic model of Toggweiler et al. (1989) also has very weak overturning of AABW (order 5 Sv) flowing into a Southern Ocean bottom water cell of substantial intensity (more than 15 Sv).

While the overturning rate of NADW increases from 14.0 Sv (with Antarctic salt) to 18.4 Sv (*without* Antarctic salt, and with an outflow of Mediterranean Sea water), the *outflow* rate into the Southern Ocean is only marginally affected; there is 1.2 Sv more inter-ocean exchange of NADW (Table 4). The increased rate of NADW production in experiment XI has a strong effect on the Deacon cell. So far we have witnessed the sensitivity of the Deacon cell to changes in the Drake Passage bathymetry (experiment V) and changes in the level of horizontal diffusion (experiment VI). In the present experiment, more of the equatorward wind-driven flow in the upper branch of the Deacon cell is ultimately drawn northward at intermediate depths, either flowing into the NADW overturning cell, or returning southward after only a brief excursion into the Atlantic basin (Fig. 16a,b).

The largest-scale response of the World Ocean water masses to cutting off the wintertime Antarctic salinity adjustment is shown in Table 3. The bottom and deep water freshens and warms in the absence of deep convective overturn and isopycnal mixing of cold saline AABW. The deep water is now only slightly too cold, but it has become far too fresh. Annual mean models without any Antarctic salt adjustment are characteristically too fresh in the deep levels, and typically show no signs of an AAIW minimum (e.g., Toggweiler et al. 1989; Hirst and Godfrey 1993). This extends to coupled ocean-atmosphere models without enhanced Antarctic salinities (England 1992a). The present ex-



upwelling of saline AABW, its overall structure is maintained. In view of the results of similar ocean GCMs (e.g., Toggweiler et al. 1989), it must be the isopycnal mixing that maintains a weak AAIW minimum in experiment XI. A detailed evaluation of the salt balance through the intermediate and deep model levels confirms this.

*j. Mixed boundary conditions experiment  
[experiment XI (mixed)]*

Given that experiment XI (restoring) is both too fresh and too cold in the bottom and deep levels of the model, it would seem that the production rate and interocean exchange of NADW remains too weak. In an idealized single-basin geometry, Weaver and Sarachik (1991) have recently shown that a model that is stable under *restoring* boundary conditions can become unstable upon a switch to *mixed* boundary conditions. In particular, they find that their deep thermohaline overturning adjusts strongly and continuously when mixed boundary conditions are adopted. In a sense, their single-basin domain is an idealized North Atlantic, with rectangular geometry and high-latitude thermohaline overturning of dense water. In view of their findings, it seems appropriate to consider experiment XI under a switch to mixed boundary conditions. As was discussed earlier, mixed boundary conditions are physically more acceptable than restoring boundary conditions because there is negligible direct feedback between surface salinities and evaporation/precipitation.

Because our geometry and surface boundary conditions are realistic, and in particular, because our model includes multiple sources of deep water, there is no guarantee that the findings of Weaver and Sarachik (1991) will be replicated. Indeed, several studies (e.g., Maier-Reimer and Mikolajewicz 1989; Toggweiler and Samuels 1992) have found that a spun-up conveyor belt (under restoring boundary conditions) remains stable upon a switch to mixed boundary conditions.

To switch from experiment XI (restoring) to experiment XI (mixed) we first diagnosed the *implied* freshwater flux during a 50-year integration of the restoring boundary conditions run. The averaged freshwater flux during the 50-year integration was saved and used as the *fixed* flux boundary condition in experiment XI (mixed); that is, there is no abrupt change in the surface forcing conditions in the switch from restoring to mixed boundary conditions. However, the mixed boundary conditions experiment proceeds without any reference to the Levitus (1982) surface salinities, and so strong fluctuations in the surface density field (and hence thermohaline overturning) can develop (e.g., Bryan 1986; Weaver et al. 1991).

Experiment XI (mixed) was initially run out for 400 surface years, with frequent diagnosis of the critical

thermohaline overturning parameters such as NADW overturning and outflow and AABW overturning. During the 400-year integration there were no abrupt changes in the component of thermohaline circulation (such as the *polar halocline catastrophe* of Bryan 1986; or the violent overturning *flushes* of Weaver and Sarachik 1991). Furthermore, the overturning and outflow rate of NADW remained extremely steady (Table 4), with only small (order 0.1 Sv) fluctuations observed. In contrast, the thermohaline cell adjacent to Antarctica initially intensifies to around 23 Sv, and then begins to settle back toward more moderate values (Table 4). Furthermore, the northward flow of bottom water in the deep Southern Hemisphere thermohaline cell strengthens to 22.8 Sv. Overall, switching to mixed boundary conditions in experiment XI primarily alters the thermohaline circulation in the Southern Ocean (e.g., the ACC intensifies by more than 30 Sv).

In spite of these findings, it should be noted that this experiment was by no means run out to a steady state. However, Toggweiler and Samuels (1992) run a similar experiment for a longer period (1000 surface years) and they too find negligible adjustment in NADW production, unless their Southern Hemisphere winds are weakened substantially (leaving the ocean state out of balance with the surface forcing).

*k. Seasonal North Atlantic experiment (experiment XII)*

In experiment XII, we recognize the importance of the seasonal cycle in temperature and salinity in determining the World Ocean deep water masses, and in particular, the formation of NADW. With the exception of the salt adjustment off Antarctica, the present study has been run under *annual*-mean conditions, without any seasonal oscillation in surface forcing. By including seasonal variations in the North Atlantic, the surface waters will reach a denser (wintertime) state, and the corresponding thermohaline overturning should intensify. It is worth mentioning that a version of the World Ocean model is presently being run with a complete seasonal cycle in surface conditions (i.e., temperature, salinity, and wind stress). The results of that experiment will be presented in a future report. For now, experiment XII serves to highlight the role of seasonal North Atlantic thermohaline forcing in capturing realistic levels of NADW production.

Global-mean profiles of temperature and salinity indicate a strong response to the introduction of seasonal thermohaline forcing in the North Atlantic (Table 3). The model's bottom water becomes both warmer and saltier in response to the enhanced production of NADW in experiment XII. The globally averaged vertical profile of salinity shows two relative maxima (one in the upper thermocline, the other at 2228 m), as well as an intermediate depth minimum (at 754 m). This

complicated vertical salinity structure is a feature of the observed global ocean (Table 3b; Levitus 1982). Most coarse-resolution World Ocean models only simulate monotonically freshening conditions in the vertical. The correct representation of the subtle vertical layering of deep and intermediate water masses represents a major success for the present model.

The global and basinwide meridional overturning and salinity distributions in experiment XII are presented in Fig. 17. The maps shown in this figure correspond to the annual mean state of the model during the final ten years of integration. Seasonal variations in the North Atlantic are confined to the first few surface levels, with negligible fluctuation in the deep thermohaline overturning of NADW. The actual *overturning* rate in the North Atlantic has marginally increased from experiment XI, up 4.3 Sv (or about 20%). However, the *outflow* rate has increased substantially from 8.6 Sv to 12.6 Sv (or 45%), indicating a stronger interocean exchange of NADW. This is evident in the  $T$ - $S$  sections and total northward heat transport in experiment XII. The modeled deep and bottom water becomes both warmer and saltier in each ocean basin. The Atlantic basin 34.80 psu isohaline now spreads into the Southern Ocean quite realistically (cf. Figs. 2 and 17c), whereas previously it had been confined to the surface 2500 m in the North Atlantic (Fig. 16c). With enhanced thermohaline overturning in the North Atlantic, the poleward heat transport becomes more symmetric about the equator (Fig. 7).

The higher outflow of NADW is transported into the Indian and Pacific basins via the ACC. Differenced  $T$ - $S$  sections between experiment XII and experiment XI (not shown) indicate a maximum salinity response in the core of the deep ACC in the Indian Ocean at about 2200 m. This is subsequently advected and diffused northward into the deep Indian Ocean and eastward into the Pacific basin. The increased deep densities in the Pacific Ocean restore the tongue of AAIW that had been missing in experiment XI (Fig. 16e). This is reminiscent of how the increased AABW salinity in experiment IV had formed a sufficiently dense bottom layer to provide buoyancy, and in turn limit the low salinity waters to intermediate levels.

With an increased outflow of NADW in experiment XII, continuity of mass requires an increased inflow. Given the uncertainty as to exactly how NADW eventually returns to the North Atlantic, it is interesting to attempt to trace the path of flow preferred by the increased component of NADW outflow in experiment XII. Simply studying maps of differenced circulation does not resolve this problem, because the ACC weakens dramatically in response to enhanced NADW production (explained below). The use of idealized tracers of North Atlantic surface water would probably provide the best insight into this problem, and future calculations are planned to this effect.

The weakening of the ACC in experiment XII (by

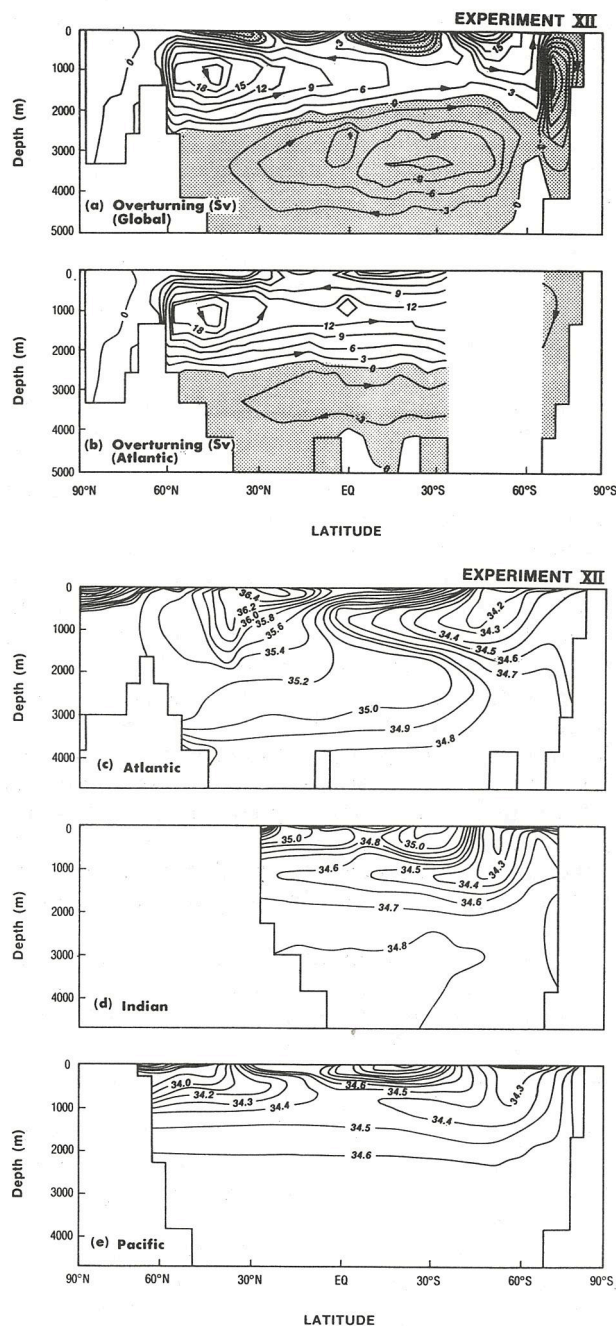


FIG. 17. As in Fig. 16 but for the seasonal North Atlantic experiment (experiment XII).

43 Sv, Table 4) must be due to adjustments in the deep density field either side of the Drake Passage gap, because there has been no change in the wind-stress forcing since experiment X. Examination of water mass properties on either side of the Drake Passage sill confirms this. Before we included a seasonal thermohaline cycle in the North Atlantic (i.e., experiment XI), the water on the Atlantic side of the Drake Passage sill is very cold ( $-1.4^{\circ}\text{C}$ ) and reasonably saline (34.50 psu)

and, hence, somewhat denser than the water on the Pacific side of the sill ( $0.8^{\circ}\text{C}$ ,  $34.36$  psu). This results in a strong JEBAR component of throughflow in the Drake Passage. However, when NADW production is enhanced, the pressure difference across the sill weakens; with the increase in the Atlantic water density ( $-0.4^{\circ}\text{C}$ ,  $34.68$  psu;  $\Delta\rho = 0.105 \text{ kg m}^{-3}$ ) being outweighed by the increase in the Pacific water density ( $1.0^{\circ}\text{C}$ ,  $34.60$  psu;  $\Delta\rho = 0.180 \text{ kg m}^{-3}$ ). The net effect is a reduction in the Drake Passage throughflow and hence the ACC. In their global ocean model, Mikolajewicz and Maier-Reimer (1990) find that the strength of the ACC is negatively correlated with the outflow rate of NADW. This dependence is also apparent in the present study.

Because the increased NADW outflow affects the Pacific water just west of the Drake Passage sill, it seems reasonable that some or even all of the enhanced NADW outflow returns via the Drake Passage (as in previous experiments). However, changes in the Indonesian Passage throughflow and Agulhas leakage indicate that some of the NADW is adhering to the thermohaline conveyor belt of Gordon (1986) and Broecker (1991). For example, the increased NADW outflow strengthens the Indonesian throughflow by about  $1.5 \text{ Sv}$ . More importantly, the Agulhas leakage in the surface  $1347 \text{ m}$  increases from  $1.2 \text{ Sv}$  to  $2.9 \text{ Sv}$  (though it should be noted that at coarse resolution the model cannot realistically simulate an Agulhas leakage of warm-core eddies). In effect, the enhanced outflow returns in part via a "warm water route" (i.e., with the Agulhas leakage) and in part via the Drake Passage "cold water route."

## 5. Overview and conclusions

A series of coarse-resolution World Ocean experiments have been diagnosed in terms of the model's representation of the global-scale water masses. The original goal of this study was to determine whether the standard ( $3.75^{\circ}$  longitude,  $4.5^{\circ}$  latitude) GFDL ocean climate model could resolve the World Ocean water-mass configuration at its largest scale. Given the inferior representation of  $^{14}\text{C}$  in the GFDL ocean climate model in a robust diagnostic mode (Toggweiler et al. 1989), it was hoped that a reasonable simulation of intermediate and deep water masses could be achieved without the use of any internal restoring terms in the prognostic equations for temperature and salinity. Furthermore, given the computational effort required to integrate higher-resolution global models to a truly steady state, it was decided that the experiments would be run with a standard coarse resolution. It will be some time into the future before high-resolution ocean models are coupled to GCMs of the atmosphere in order to study global climate. Even then, these models face their own problems when it comes to the dynamics of the ACC and the Drake Passage throughflow.

By maintaining coarse resolution throughout the present study, we have been able to invest computational power into integrating a variety of model configurations to genuinely steady states.

While requiring a substantial computational effort, the technique of successively upgrading model configurations has the advantage of isolating key processes or forcing conditions critical for the resolution of certain water masses. In terms of the so-called "global-scale" water masses, we ultimately find sufficient conditions for their representation in the GFDL ocean climate model. In particular, the simulation of saline Antarctic Bottom Water requires a wintertime salt flux adjustment (to the standard climatological boundary conditions) in the Ross and Weddell seas. In a more recent model run with a complete seasonal cycle in surface forcing, we find that a wintertime salinity enhancement is still necessary for AABW representation. This adjustment crudely simulates the process of brine release when sea ice formation rejects salt into the water column.

The resolution of Antarctic Intermediate Water in multilevel ocean models appears to depend on a number of factors. First, the density of the model's deep layers should be sufficiently high to provide buoyancy for any potential intermediate water. Ocean models run with only annually averaged forcing conditions are characteristically too warm and fresh (and hence, too buoyant) near the bottom (England et al. 1992). Without sufficient density at great depth, water of mid-latitude origin tends to ventilate the very deep model levels (e.g., Fig. 4). A second factor is model geometry, and in particular, the choice of the location of the Drake Passage gap relative to the polar westerly wind belt. If the Drake Passage gap artificially infringes well into the latitude belt of the circumpolar westerlies, a dynamical constraint in the barrier-free zone dictates that the surface Ekman drift return as a deep poleward flow. On completing this circulation, the intensity of downwelling through the model's intermediate levels may be too great to accommodate equatorward AAIW flows (e.g., experiment IV). Furthermore, in a narrow Drake Passage configuration, the coast of Southern Chile confronts an eastward geostrophic flow of cold fresh Subantarctic Water, forcing downwelling and convective overturn of surface waters, which ultimately renew AAIW in the model (England et al. 1993). Had the Drake Passage been wider in such circumstances, it is possible that this renewal process would be lost to an enhanced Drake Passage throughflow. Yet another factor determining the quality of AAIW representation is the choice of closure scheme that approximates the (implicit) mesoscale mixing of temperature and salinity. For example, we saw in one experiment (experiment IX) how enhancing Cartesian mixing rates in an alongisopycnal sense brings more fresh water from the surface into intermediate levels. On the other hand, with excessive levels of lateral diffusion, an approximate

balance between vertical advection and horizontal diffusion dictates intense vertical motions in the so-called Deacon cell. Furthermore, high lateral diffusion rates imply a rapid blending of surface  $T$ - $S$  conditions, making it difficult for vertical motions and convective adjustment to transport genuine surface properties downward. In all, capturing an AAIW minimum appears to be dependent on the model geometry in the Drake Passage, the choice of lateral diffusion schemes, and the relative buoyancy provided by the simulated deep water.

Contrasting the sensitivity of AAIW to the overall model configuration, the formation of North Pacific Intermediate Water appears to be relatively straightforward to resolve in primitive equation models. Even with excessive levels of lateral diffusion (e.g., experiment IV), NPIW appears so long as saline deep waters ventilate the North Pacific Ocean. The saline deep water can originate from either high salinity Antarctic shelf water (e.g., experiments IV–VI), or from the North Atlantic Ocean (e.g., experiment XII). A low lateral diffusion rate (experiment VI) does improve the representation nevertheless.

The correct simulation of North Atlantic Deep Water overturning (and outflow into the Southern Ocean) appears to be primarily dependent on the density of North Atlantic surface waters (e.g., experiments VII and XII). However, the NADW production rate also appears to be controlled to an extent by the density of bottom water formed in the extreme Southern Ocean (e.g., experiments VII, IX, XI). This is related to the thermohaline circulation in the model (experiment II, Fig. 4b); there is a tendency for water north of the Drake Passage gap to be drawn poleward toward the region of AABW formation, in spite of the dynamical constraints restricting meridional flows in the barrier-free zone. The water eventually reaches the Antarctic overturning by downwelling at the Drake Passage gap and flowing geostrophically across the deep sill. Within this scheme, intense Antarctic Bottom Water overturning can limit the inflow of water across the latitude of the southern tip of Africa, ultimately restricting the outflow rate of NADW. In a similar manner, the strength of the westerly wind belt at the latitude of Cape Horn might determine NADW outflow rates by controlling the amount of upper-ocean inflow into the Atlantic basin (Toggweiler and Samuels 1992). Evidence for this notion was also found in the present study (experiment X).

Apart from monitoring the global-scale water-mass structure simulated in each experiment, we have also analyzed several critical features that characterize the ocean circulation at its largest scale. For example, the poleward transport of heat in the ocean responds to changes in the production rate of NADW (Fig. 7). It was also seen that the southward heat transport across the ACC scaled with the level of lateral diffusion em-

ployed by the model. This is related to a spurious diapycnal diffusion of meridional temperature gradients if excessive levels of horizontal diffusion are used.

Calculations of the direct westward flow from the Agulhas Current into the Atlantic basin (i.e., Agulhas leakage) reveal the tendency for eastward drift past the Cape of Good Hope when the Indonesian Passage is closed. On resolving the Indonesian throughflow, a weak Agulhas leakage of 0.5 Sv develops in the surface 1347 m, strengthening to as much as 2.9 Sv when NADW production is enhanced (experiment XII). The question of NADW return flow is difficult to address in coarse-resolution models because in reality the Agulhas leakage depends on subgrid-scale eddies to propagate warm water westward. This partially explains why we find the return path of NADW to be primarily via a "cold water route" (i.e., the Drake Passage), although strong NADW formation sees some return flow via the Agulhas leakage (i.e., the "warm water route").

The series of experiments presented here provide insight into the nature of the World Ocean circulation at its largest scale. In addition, they are a useful reference for determining the appropriate model configuration for resolving the global-scale water masses in coarse-resolution models. Given the critical role that primitive equation ocean models play in the study of global climate, it is important that the ventilation processes and large-scale transports of heat and fresh water be properly represented. Even in a purely prognostic configuration, there is no guarantee that the model with a superior representation of water masses will produce the most realistic ventilation of the ocean interior. However, poor representation of deep and intermediate water masses generally indicates erroneous features in the modeled ocean circulation. Future calculations will assess the representation of geochemical tracers in some of the experiments previously described above.

*Acknowledgments.* The World Ocean experiments were run on the CSIRO Y-MP Cray with the financial support of a CSIRO INRE Postgraduate Project Award. Tony Hirst, Matthias Tomczak, and Stuart Godfrey gave helpful criticisms of the original manuscript. Correspondence with Kirk Bryan, Andrew Weaver, and Robbie Toggweiler on certain aspects of this study is gratefully acknowledged. The very high horizontal diffusion case (discussed in section 4d) was provided by Bonnie Samuels at the GFDL. Ron Stouffer kindly provided access to certain GFDL climate model output, including data from the Manabe and Stouffer (1988) and Manabe et al. (1991) climate models. Two anonymous reviewers are acknowledged for constructive criticism of the original manuscript.

## REFERENCES

- Baumgartner, A., and E. Reichel, 1975: *The World Water Balance*, Elsevier, 179 pp.

- Broecker, W. S., 1991: The great ocean conveyor. *Oceanogr.*, **4**, 79–89.
- Bryan, F., 1986: High latitude salinity effects and interhemispheric thermohaline circulations. *Nature*, **323**, 301–304.
- , 1987: Parameter sensitivity of primitive equation ocean general circulation models. *J. Phys. Oceanogr.*, **17**, 970–985.
- Bryan, K., 1969: A numerical method for the study of the circulation of the World Ocean. *J. Comput. Phys.*, **3**, 347–376.
- , 1979: Models of the World Ocean. *Dyn. Atmos. Oceans*, **3**, 327–338.
- , 1984: Accelerating the convergence to equilibrium of ocean-climate models. *J. Phys. Oceanogr.*, **14**, 666–673.
- , and L. J. Lewis, 1979: A water mass model of the World Ocean. *J. Geophys. Res.*, **85**, 2503–2517.
- Carmack, E. C., and T. D. Foster, 1975: On the flow of water out of the Weddell Sea. *Deep-Sea Res.*, **22**, 711–724.
- Cox, M. D., 1984: *A primitive equation, three-dimensional model of the ocean*. GFDL Ocean Group Tech. Rep. No. 1, 143 pp.
- , 1987: Isopycnal diffusion in a z-coordinate ocean model. *Ocean Model.*, **74**, 1–5.
- , 1989: An idealized model of the World Ocean. Part I: The global scale water masses. *J. Phys. Oceanogr.*, **19**, 1730–1752.
- Cummins, P. F., 1991: The deep water stratification of ocean general circulation models. *Dyn. Atmos. Ocean*, **29**, 563–575.
- England, M. H., 1992a: On the formation of Antarctic Intermediate and Bottom Water in ocean general circulation models. *J. Phys. Oceanogr.*, **22**, 918–926.
- , 1992b: The global-scale circulation and water-mass formation in a World Ocean model. Ph.D. thesis, University of Sydney, 226 pp.
- , M. Tomczak, and J. S. Godfrey, 1992: Water-mass formation and Sverdrup dynamics: A comparison between climatology and a coupled ocean-atmosphere model. *J. Mar. Sys.*, **3**, 279–306.
- , J. S. Godfrey, A. C. Hirst, and M. Tomczak, 1993: The mechanism for Antarctic Intermediate Water renewal in a World Ocean model. *J. Phys. Oceanogr.*, **23**, 1553–1560.
- Esbenson, S. K., and Y. Kushnir, 1981: The heat budget of the global ocean: An atlas based on estimates from surface marine observations. *Clim. Res. Institute Rep. No. 29*, Oregon State University, 27 pp.
- Foster, T. D., and E. C. Carmack, 1976: Frontal zone mixing and Antarctic Bottom Water formation in the southern Weddell Sea. *Deep-Sea Res.*, **23**, 301–317.
- Gill, A. E., and K. Bryan, 1971: Effects of geometry on the circulation of a three-dimensional Southern-Hemisphere ocean model. *Deep-Sea Res.*, **18**, 685–721.
- Godfrey, J. S., 1989: A Sverdrup model of the depth-integrated flow for the World Ocean allowing for island circulations. *Geophys. Astrophys. Fluid Dyn.*, **45**, 89–112.
- Gordon, A. L., 1986: Inter-ocean exchange of thermocline water. *J. Geophys. Res.*, **91**, 5037–5046.
- Haney, R. L., 1971: Surface thermal boundary condition for ocean circulation models. *J. Phys. Oceanogr.*, **1**, 241–248.
- Hastenrath, S., 1980: Heat budget of tropical ocean and atmosphere. *J. Phys. Oceanogr.*, **10**, 159–170.
- Hellerman, S., and M. Rosenstein, 1983: Normal monthly wind stress over the World Ocean with error estimates. *J. Phys. Oceanogr.*, **13**, 1093–1104.
- Hirst, A. C., and J. S. Godfrey, 1993: The role of Indonesian throughflow in a global ocean GCM. *J. Phys. Oceanogr.*, **23**, 1057–1086.
- Hsieh, W. W., and A. E. Gill, 1984: The Rossby adjustment problem in a rotating, stratified channel, with and without topography. *J. Phys. Oceanogr.*, **14**, 424–437.
- Hsiung, J., 1985: Estimates of global oceanic meridional heat transport. *J. Phys. Oceanogr.*, **15**, 1405–1413.
- Isemer, H. J., and L. Hasse, 1987: *The Bunker Climate Atlas of the North Atlantic Ocean*. Vol. 2, Springer-Verlag, 252 pp.
- Jacobs, S. S., R. G. Fairbanks, and Y. Horibe, 1985: Origin and evolution of water masses near the Antarctic continental margin: Evidence from  $\text{H}_2^{18}\text{O}/\text{H}_2^{16}\text{O}$  ratios in seawater. *Oceanology of the Antarctic Continental Shelf*, Antarct. Res. Ser., **43**, Amer. Geophys. Union, 58–86.
- Killworth, P. D., 1987: Topographic instabilities in level model OGCMs. *Ocean Modelling*, **75**, 9–12. [Unpublished manuscript.]
- Levitus, S., 1982: *Climatological Atlas of the World Ocean*. NOAA Prof. Paper 13, U.S. Dept. of Commerce, Washington, DC, 173 pp.
- , 1984: Annual cycle of temperature and heat storage in the World Ocean. *J. Phys. Oceanogr.*, **14**, 727–746.
- , 1986: Annual cycle of salinity and salt storage in the World Ocean. *J. Phys. Oceanogr.*, **16**, 322–343.
- McCartney, M. S., 1977: Subantarctic Mode Water. A voyage of discovery, M. V. Angel, Ed., *Deep-Sea Res.*, **24**(Suppl.), 103–119.
- McWilliams, J. C., and coauthors, 1983: The local dynamics of eddies in the western North Atlantic. *Eddies in Marine Science*, A. R. Robinson, Ed., Springer-Verlag, 92–113.
- Maier-Reimer, E., and U. Mikolajewicz, 1989: Experiments with an OGCM on the cause of the Younger Dryas. Max-Planck-Institut für Meteorologie Rep. No. 39, 46 pp. [Reprinted from *Oceanography*, A. Ayala-Castanares, W. Wooster, and A. Yanez-Arancibia, Eds., UNAM Press, 87–100.]
- Manabe, S., and R. J. Stouffer, 1988: Two stable equilibria of a coupled ocean-atmosphere model. *J. Climate*, **1**, 841–866.
- , M. J. Spelman, and K. Bryan, 1991: Transient responses of a coupled ocean-atmosphere model to gradual changes of atmospheric carbon dioxide. Part I: Annual mean response. *J. Climate*, **4**, 785–818.
- Marotzke, J., 1991: Influence of convective adjustment on the stability of the thermohaline circulation. *J. Phys. Oceanogr.*, **21**, 903–907.
- Meehl, G. A., W. M. Washington, and A. J. Semtner, 1982: Experiments with a global ocean model driven by observed atmospheric forcing. *J. Phys. Oceanogr.*, **12**, 301–312.
- Mikolajewicz, U., and E. Maier-Reimer, 1990: Internal secular variability in an ocean general circulation model. *Climate Dyn.*, **4**, 145–156.
- Oort, A. H., and T. H. Vonder Haar, 1976: On the observed annual cycle in the ocean-atmosphere heat balance over the Northern Hemisphere. *J. Phys. Oceanogr.*, **6**, 781–800.
- Pacanowski, R. C., K. W. Dixon, and A. Rosati, 1991: *The GFDL Modular Ocean Model Users Guide Version 1.0*. GFDL Ocean Group Tech. Rep. No. 2, 46 pp.
- Redi, M. H., 1982: Oceanic isopycnal mixing by coordinate rotation. *J. Phys. Oceanogr.*, **12**, 1154–1158.
- Rintoul, S. R., 1991: South Atlantic interbasin exchange. *J. Geophys. Res.*, **96**, 2675–2692.
- Roemmich, D., and C. Wunsch, 1985: Two transatlantic sections: Meridional circulation and heat flux in the subtropical North Atlantic Ocean. *Deep-Sea Res.*, **32**, 619–664.
- Saunders, P. M., and S. R. Thompson, 1993: Transport, heat and freshwater fluxes within a diagnostic numerical model (FRAM). *J. Phys. Oceanogr.*, **23**, 452–464.
- Schmitt, R. W., P. S. Bogden, and C. E. Dorman, 1989: Evaporation minus precipitation and density fluxes for the North Atlantic. *J. Phys. Oceanogr.*, **19**, 1208–1221.
- , and K. Bryan, 1991: Mysteries of the ocean water budget. *Summary Report, 12th Session of the SCOR-IOC Committee on Climate Changes and the Ocean*. 17 pp. (Annex. IV) unpublished manuscript.
- Semtner, A. J., and R. M. Chervin, 1988: A simulation of the global ocean circulation with resolved eddies. *J. Geophys. Res.*, **93**, 15 502–15 522.
- , and —, 1991: A thermohaline conveyor belt in the World Ocean. *WOCE Notes*, **3**(2), 12–15.

- , and —, 1992: Ocean general circulation from a global eddy-resolving model. *J. Geophys. Res.*, **97**, 5493–5550.
- Stouffer, R. J., S. Manabe, and K. Bryan, 1989: Interhemispheric asymmetry in climate response to a gradual increase of atmospheric CO<sub>2</sub>. *Nature*, **342**, 660–662.
- Sverdrup, H. U., M. W. Johnson, and R. H. Fleming, 1942: *The Oceans: Their Physics, Chemistry and General Biology*. Prentice-Hall, 1087 pp.
- Thiele, G., W. Roether, P. Schlosser, R. Kuntz, G. Siedler, and L. Stramma, 1986: Baroclinic flow and transient-tracer fields in the Canary–Cape Verde Basin. *J. Phys. Oceanogr.*, **16**, 814–826.
- Toggweiler, J. R., and B. Samuels, 1992: Is the magnitude of the deep outflow from the Atlantic Ocean actually governed by Southern Hemisphere winds? *The Global Carbon Cycle*, M. Heimann, Ed., Springer-Verlag.
- , K. Dixon, and K. Bryan, 1989: Simulations of radiocarbon in a coarse-resolution world ocean model. I: Steady state prebomb distributions. *J. Geophys. Res.*, **94**, 8217–8242.
- Trenberth, K. E., 1979: Mean annual poleward energy transports by the oceans in the Southern Hemisphere. *Dyn. Atmos. Oceans*, **4**, 57–64.
- Washington, W. M., and G. A. Meehl, 1989: Climate sensitivity due to increased CO<sub>2</sub>: Experiments with a coupled atmosphere and ocean general circulation model. *Climate Dyn.*, **4**, 1–38.
- Weaver, A. J., and E. S. Sarachik, 1990: On the importance of vertical resolution in certain ocean general circulation models. *J. Phys. Oceanogr.*, **20**, 600–609.
- , and —, 1991: The role of mixed boundary conditions in numerical models of the ocean's climate. *J. Phys. Oceanogr.*, **21**, 1470–1493.
- , —, and J. Marotzke, 1991: Freshwater flux forcing of decadal and interdecadal oceanic variability. *Nature*, **353**, 836–838.
- Weiss, R. F., H. G. Ostlund, and H. Craig, 1979: Geochemical studies of the Weddell Sea. *Deep-Sea Res.*, **26**, 1093–1120.
- Welander, P., 1986: Thermohaline effects in the ocean circulation and related simple models. *Large-Scale Transport Processes in the Oceans and Atmosphere*, J. Willebrand and D. L. T. Anderson, Eds., D. Reidel, 163–200.
- Wijffels, S., R. W. Schmitt, H. Bryden, and A. Stigebrandt, 1992: On the transport of freshwater by the oceans. *J. Phys. Oceanogr.*, **22**, 155–162.
- Wüst, G., 1933: Das Bodenwasser und die Gliederung der Atlantischen Tiefsee. Teil I: Schichtung und Zirkulation des Atlantischen Ozeans. *Wiss. Ergebn. Dtsch. Atlant. Exped. "Meteor,"* **6**(1), 1–107.